Microelectromechanical Sensors and Measurements

by Darren Robert Southworth

This thesis/dissertation document has been electronically approved by the following individuals:

Van Dover,Robert B. (Chairperson)

Craighead,Harold G (Minor Member)

Parpia,Jeevak M (Minor Member)

Schwab,Keith C. (Additional Member)

MICROELECTROMECHANICAL SENSORS AND MEASUREMENTS

A Dissertation

Presented to the Faculty of the Graduate School

of Cornell University

in Partial Fulfillment of the Requirements for the Degree of

Doctor of Philosophy

by

Darren Robert Southworth

August 2010

MICROELECTROMECHANICAL SENSORS AND MEASUREMENTS

Darren Robert Southworth, Ph.D.

Cornell University 2010

Microelectromechanical systems (MEMS) are realizing their potential in many areas of pure and applied science. This dissertation presents novel sensor designs and studies toward realization of MEMS in realistic sensor applications. A parallel plate membrane is presented whose small air gaps and megahertz resonance frequency takes advantage of the gas dynamics in squeeze films to produce a pressure sensor, thereby suggesting a means of improving the quality factor (Q) of resonance in fluid. The non-linear frequency dependence to stress in a buckled beam is used to demonstrate a sensitive generic geometry for trace vapor sensing. In the fundamental study of quality factor, the uncharacteristically low dissipation (Q^{-1}) observed in silicon nitride resonators is shown to relate to film stress, suggesting a means of exploring the otherwise-inscrutable universal dissipation plateau observed in glasses. These studies demonstrate an interesting advance in application and development of MEMS.

BIOGRAPHICAL SKETCH

Born in the 13.75 billionth year of the cosmos during the 4.5 billionth year of our planet, 180 thousandth year of our species, fourth century of human understanding of nature and reality, one of seven billion others on this rare and lonely world.

Darren attended a Waldorf school during formative life, lived in Germany and Russia and studied at the University of Maine. He graduates 22^{nd} grade from Cornell University under great pressure to do something meaningful with this tremendous education.

To my teachers.

ACKNOWLEDGEMENTS

The research conducted in this thesis is the work of many hands. The incremental advancement it represents is the sharp tip of a pyramid of training and knowledge acquired by the many generations of investigators before me. Great thanks to my advisors, Jeevak Parpia, Harold Craighead, and Keith Schwab, for sharing with me some of their great knowledge and experience and for providing me with the environment in which to learn. And to my cohorts, the members of these groups past and present, my great admiration and appreciation: science is no one man show, and working with you through the unending confusion and difficulty that is graduate research has been great. I extend my warmest appreciations to the diversely talented support staff at Cornell, in the CNF, CCMR, CNS, CHESS, and Clark Hall in general; you make our research possible. To my parents I must extend my greatest thanks. Your unwavering dedication to my education has been an incomparable gift, and it will always remain my goal to use it to its fullest and share it with others. Finally, a broad thank you to our sources of funding and to the entire population that supports them. Thank you all.

TABLE OF CONTENTS

LIST OF TABLES

LIST OF FIGURES

CHAPTER 1

INTRODUCTION

1.1 Microelectromechanical Sensors

This thesis presents a study in application of resonant microelectromechanical systems (MEMS). This broadly defined area of investigation has seen great technological advancement in the preceding decades, leading to the development of modern micromirror arrays for light projection, radio frequency switches, and others. A notable aspect of MEMS is their potential as sensors [1]. The characteristic changes in behavior associated with dimensional reduction make MEMS appealing candidates: Their low mass leaves their behavior susceptible to small forces. Their high surface to volume opens surface effects to exploitation. In resonant structures, evidence for changes in behavior is often amplified by a factor of Q, the mechanical quality factor, and with their high natural resonance a small percentage change in frequency can be of significant absolute value.

The obvious advantages of resonant micromechanical sensors are checked by number of practical challenges. The interaction of a tiny, high frequency structure with its environment can be complicated, and the very attributes that confer their great sensitivity can make microstructures susceptible to many other influences. In devices with small dimensions and high resonance frequencies, for example, interaction with the ambient gas involve aspects of fluid mechanics that are not relevant in macroscopic objects. The effect of surface interactions are likewise amplified since surface-to-volume ratio scales inversely with size. The greater role of surfaces in the overall behavior is a good example of the variables that must be understood and controlled, but could also be exploited.

Developments in understanding of many aspects of the interactions between

micromechanical resonators and their environment will be necessary in order to take advantage of the advantageous attributes of microelectromechanical systems.

And there may be many new ideas lurking in the details.

1.2 Micromechanical Sensors in Gas

Microscale sensors, with typical dimensions on the order of 10^{-6} m, are relatively new to the world of sensing. A few prominent commercial applications have now been developed to the level of marketability, most notably force sensors (accelerometers) for automotive airbags and entertainment systems. Resonant sensors that operate in ambient conditions, however, have not yet been developed. Operation of resonant MEMS in gas affords a particular challenge, but if atmospheric operation can be made viable then microresonators may contribute valuable new technology.

Gas interactions with MEMS has been an active area of study since the development of micromechanics, and the large existing body of knowledge is still expanding. Extended reference is provided in Chapter 3. In vacuum, material-dependent- and clamping losses dominate the quality factor, Q, which is on the order of $10^3 - 10^5$, (or 10^6 in highly stressed structures). At low very low pressures the mean free path of gas molecules is much larger than device dimensions, and energy is lost to collisions with individual molecules. As such, a linear dependence of the Q is found in this "molecular flow regime." At higher pressures, when typical device dimensions are greater than a few mean free paths, the molecular flow regime gives way to viscous flow, and gas interactions become a primary mode of energy loss to the vibrating system. The dissipation Q^{-1} in this regime scales as $P^{-\frac{1}{2}}$, and quality factors at atmospheric pressures are commonly on the order of $10^0 - 10^2$. The viscous flow regime then extends to atmospheric pressure, making this fluid regime of primary relevance for MEMS sensors operating in ambient

conditions.

In our studies the quantity of interest during sensing is the resonance frequency, where frequency variation constitutes the sensor signal. In extracting the resonance frequency, the center position of the amplitude peak must be determined (or equivalently the frequency of the maximum slope in phase). Thus the width of the resonance peak is focal to the error in the frequency determination. As such, the tremendous potential sensitivity of resonant MEMS sensors is limited in air by viscous losses and the associated broadening of the resonance. Methods of engineering low-loss structures are essential to progress of the discipline.

In Chapter 3 of this thesis, we present a structure whose interactions with ambient gas make use of dimensional scaling in MEMS. A circular membrane separated by a small distance from the substrate is shown to trap the gas present between the two in an elastic film. The entire film is located within the viscous penetration depth, the region of air in laterally static contact with the adjacent surfaces. Aside from contributing a pressure-dependent restoring force, creating a positive pressure dependence of the resonance frequency, trapping the gas film limits viscous flow, in principle depressing that primary energy loss mechanism. This presents an intriguing potential avenue to improvement of Q in air.

1.3 Stress and Surfaces in Micromechanics

Another characteristic of the reduced dimensions in microstructures is the heightened stress caused by a given magnitude of force, F, from the definition $\sigma = \frac{F}{A}$, where A is the cross-section of the mechanics and tiny. Large stresses are common in thin film structures. Stress in thin films originates from growth dynamic (arrangement of free surfaces during growth) and from thermal contraction of the materials involved. (Also from lattice mismatch, in very thin films.) An example

of the former is Volmer-Weber growth, or island growth, which is common in low pressure chemical vapor deposition: the surface forms as add-atoms pack into two-dimensional clusters (islands) that collide as they grow to form the final film. The free energy is greatest at the edge of the islands due to dangling bonds, and until the islands snap together they repel one another, leading to compressive stress in films. As such a film thickens, stress associated with Volmer-Weber growth quickly lose significance compared to the bulk. Thermal stresses arise whenever high temperature materials are deposited (e.g. thermal evaporation) or when deposition on a substrate is performed at high temperature and then cooled.

Ceramic materials are brittle and fail by fracture, where stress is concentrated at the propagating crack tip. Thin ceramic films, such as those used in this thesis, however, are capable of withstanding tensile stresses far greater than can be applied to the bulk material. This is due to the very thinness of the film. In sufficiently thin films, defects cannot become deep enough to concentrate sufficient stress at the crack tip to sustain crack propagation. Thus high quality, high stress films such as the stoichiometric silicon nitride discussed in Chapter 4 withstand film stresses in excess of a GPa, where their tensile breaking strength of the bulk is five times lower.

In high-stress films ($\sigma > 1$ GPa) of Si_3N_4 quality factors in excess of 10^6 have been measured in vacuum, as discussed in detail in Chapter 5. This low dissipation can be definitely attributed to stress, despite the current incomplete understanding as to its origin. The tremendous advantage of low inherent dissipation is very relevant to vacuum applications, and when understood and used in conjunction with the viscous damping suppression proposed in Section 1.2 could be an important factor in realization of high-Q atmospheric-pressure sensors.

At the low stress limit, stress may play a different role in sensors' development.

A new family of sensors has arisen in the literature on the subject of trace vapor sensing, as expounded upon in Chapter 4. In these mechanical sensors, changes in the properties of a sensitive surface coating is revealed in the shift in resonant frequency or static conformation. These surface coatings, themselves representing a body of literature, are intended to respond to a specific analyte—specificity being the a central challenge in the field.

In sufficiently small structures, small changes in the surface characteristics can have detectably large impacts on the device behavior. Detection of three mechanical reactions of the surface coating have been demonstrated in the literature: In static cantilevers where one surface is sensitized, swelling and contracting of a coating leads to an unbalanced stress causing static deflection of the structure. In resonant cantilevers a change in resonance frequency is based on adsorption of mass, which increases the inertia and decreases the frequency, or on changes in the Young's modulus of the surface coating, which alters the total stiffness of the beam.

However, in Chapter 4 we demonstrate a sensor geometry in which changes in the stress of a surface coating alters the frequency of a resonant, doubly-clamped structure. We show that the frequency response to the change in stress in low-stress structures, specifically doubly-clamped structures loaded to reside in the vicinity of their critical buckling load, overwhelms the frequency changes due to added mass or changes in structural stiffness. As such, stress-tuning of doubly clamped beams is shown to be a generic and highly sensitive platform for sensing surface stress variation, and therefor for trace vapor sensing.

1.4 Completing the Sensor

A key component in any future deployment of resonant micromechanical sensors must be a system by which the resonance frequency shifts can be detected. Readout schemes for applied sensor technology must be compact and robust. Practically, resonators must interface with electronics, and an electrical detection scheme is best suited. Considering the potential of simultaneously fabricating micromechanics and their associated readout electronic (amplifiers, signal processors), and thus the potential for sensor-integrated-circuits (SICs), development of fully electrical schemes is of central importance to the deployment of MEMS as real-world sensors.

Electrical transduction of mechanical motion can be accomplished though a number of mechanisms, including the piezoresistive effect, the piezoelectric effect, and capacitive coupling. In capacitive detection, the vibrating element acts as one electrode of a capacitor with a static member (or the substrate) acting as the other. Such "mechanical capacitors" are described in electrical terms in Chapter 2 and may be treated as a radio frequency circuit element. Variation in the electrode spacing of this electromechanical element provides a small, time-varying capacitance, and electrical schemes must contend with the practical challenges detection of such small signals entail.

Compact and simple designs for such a scheme have begun to be realized. A particularly low power technique based on power reflected from a MEMS has been recently developed, and is described in Chapter 2 and variously applied to several prototype sensor systems.

Access to micromechanical system entirely through the electrical domain (as apposed to optical, magnitomotive, and mechanical drive and detection schemes) opens many experimental possibilities. Ambient temperature, readout without line-of-sight, and bench-top operation, to account for practical considerations.

Compatibility with mixing, quantitative assay, and versatile applicability are valuable experimental advantages. The relative ease of implementation of this new readout genre commend it to both experimental research and to eventual sensor application.

Practical application of electrical detection of MEMS resonance is discussed in Chapter 2 of this thesis. We demonstrate this capacitive reflection technique in a number of applications, including sensing of mass addition to a resonator and detection of changes in ambient gas pressure (the subject of Chapter 3). We demonstrate integration of the detection scheme onto probes for non-traditional device detection, and show the comparability of the technique with parametric pre-amplification.

1.5 Big Plans for Tiny Structures

This thesis represents contributions to the greater task of developing micromechanical sensor technology. Looking ahead to a unification of these varied projects, one could imagine a resonant sensor surrounded by an open cavity thinner than the viscous penetration depth of the resonator, buoying its quality factor in air. This sensor, perhaps an array of coating-sensitized structures, respond to a chemical in the air and experience a shift in resonance frequency. This frequency shift is read out and a signal is transmitted to a signal recognition system, all from a platform smaller than a dime.

Sensors based on resonant MEMS are still at an early stage of development. If the inherent sensitivity of these structures, through continued effort an innovation, can be realized in the turbulent and imperfect environments in which sensors are needed, then batch fabrication and integration could make the resulting technology inexpensive and widely applicable. It is the hope of the author that these efforts

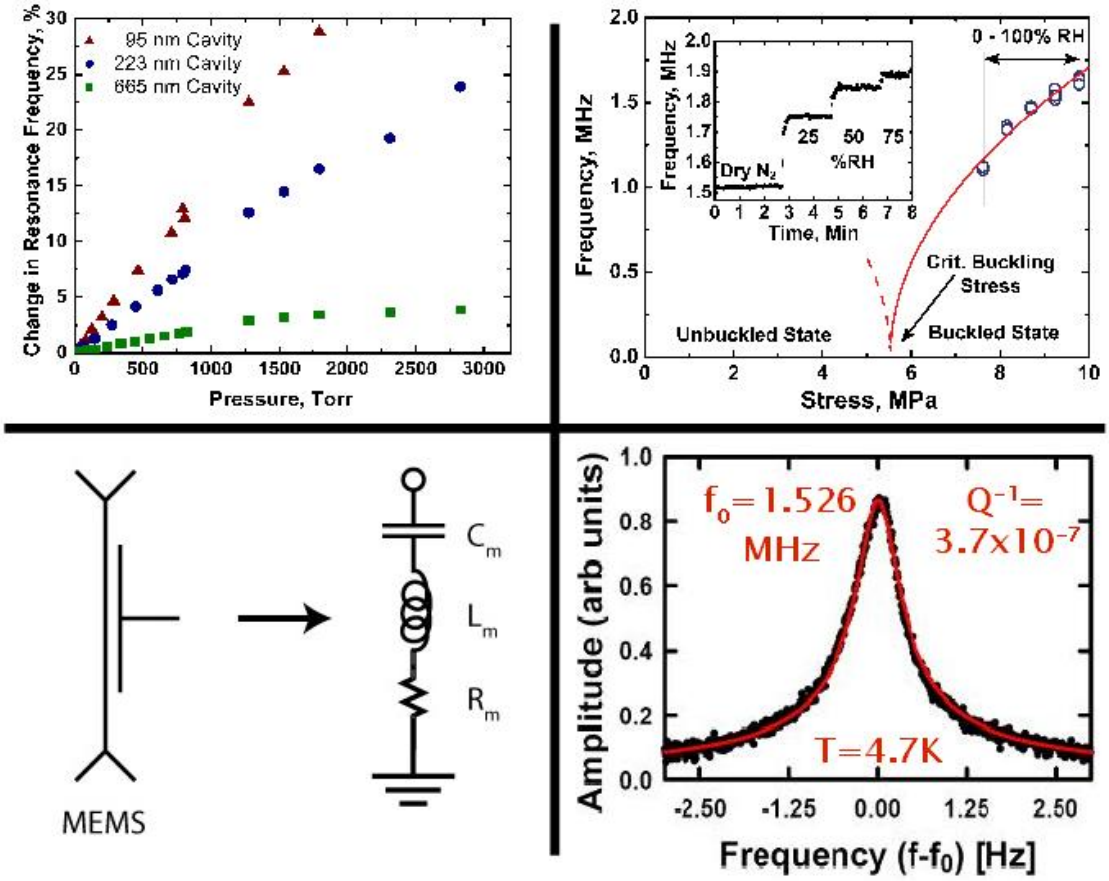

Figure 1.1: A pictorial summary of the research presented in this thesis.

will assist in bringing this new and hopeful area of study closer to real-world application.

1.6 Layout of Thesis

In Chapters 3 and 4 of this thesis we investigate two sensor designs that take advantage of scaling in micromechanical systems. Both sensors, either based on shifts in the resonance frequency of megahertz resonators, respectively transduce changes in gas pressure and variations in surface stress. Chapter 5 investigates the relationship between stress in glassy silicon nitride and the low dissipation observed

in the material, and shows that the application of stress causes deviation from the low-temperature behavior otherwise universally observed in glassy systems. This thesis begins in Chapter 2 with a description of an electrical technique for detection of micromechanical resonances, a method developed previously [2], that the author hopes will be of continues practical value to graduate students pursuing micromechanical research in the laboratory.

BIBLIOGRAPHY

[1] H. G. Craighead, Science **290** 5496 1532-1535 (2000)

[2] Patrick A. Truitt and Jared B. Hertzberg and C. C. Huang and Kamil L. Ekinci and Keith C. Schwab, Nano Letters **7** 1 120-126 (2007)

CHAPTER 2

ELECTRICALLY ADDRESSABLE MICROMECHANICS

2.1 Motivation for Electrical Detection of Micromechanical Resonance

Development of electrical readout of micromechanical resonance is important and valuable in both applied and pure research. The excellent noise characteristics of capacitive measurements have enabled experiments based on capacitive coupling between a micromechanical element and an electrode in which position detection is limited by quantum uncertainty [1, 2]. In sensors, miniaturization of capacitively detected micromechanics has already given rise to development and wide application of MEMS-based accelerometers and gyroscopes. Simple detection of capacitively-coupled high frequency MEMS has the potential to enable a new class of resonant sensor technology.

Despite the simplicity of the basic operation principle, the extremely small capacitances found in microfabricated structures lead to several practical difficulties. Since typical capacitances are measured in femtofarads, accurate measurements of the order-of-magnitude-smaller *changes* in capacitance is not trivial.

However, in both research and practice electrical detection of mechanical motion offers distinct advantages over other common readout methods. Optical interferometry and magnitomotive readout require macroscopic infrastructure (with exceptions [3]), while in principle readout electronics and micromechanics could ultimately be cofabricated. In applied technologies, this point makes electrical readout schemes most viable.

Electrical sensing by piezoelectric transduction is an alternative to capacitive methods, and has been demonstrated in microscale devices [4]. The advantages

of piezoelectric sensing over capacitive measurements include the relative ease of implementation, for example using a Wheatstone bridge; and the relative robustness, usually not requiring hermetic packaging in DC applications such as pressure (force) sensors based on membrane deflection. However resistance measurements are inherently noisy and commonly strongly temperature dependent, commending development of capacitive methods of device readout.

Capacitive readout of mechanical motion, then, represents a technologically and experimentally relevant area of research and development. In the following sections, a capacitive readout method is described in which micromechanics are directly coupled to an electrical circuit, and the resultant motion is ascertained through assay the electrical impedance match between the micromechanics and macroscale electronics, in an application of previous research [5]. Capactive readout of motion through impedance matching represents and extremely efficient and sensitive method resonance detection.[1]

2.2 Derivation: Micromechanics as a Circuit Element

2.2.1 Equations of Motion

The relevant mathematical quantities for a micromechanical resonator capacitively coupled to an electrical system are here derived. The electrical analog of micromechanics in a parallel plate configuration is the series LRC circuit depicted in Figure 2.1. The equation of motion may written

[1]This chapter presents an example of the method developed in the research of P. A. Truitt, J. B. Hertzberg, C. C. Huang, K. L. Ekinci, and K. C. Schwab, *Efficient and sensitive capacitive readout of nanomechanical resonator arrays*, published in Nano Letter [5]. Several applications are demonstrated in this chapter. It is the hope of the author that this presentation will ease the entry of future graduate students into this line of research, encouraging continued development and deployment of the method.

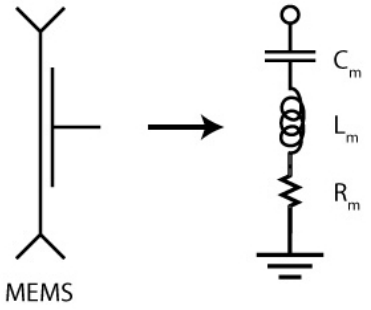

Figure 2.1: Equivalent circuit model for a capacitively coupled microelectromechanical resonator (parallel gate capacitance not depicted). Far from resonance the MEMS acts as an open circuit. Resonance is modeled with the motional inductance and capacitance, (L_m and C_m), forming an effective short circuit, introducing the motional impedance, R_m, to the electrical system.

$$F = m\ddot{x} + \dot{x}\gamma + kx. \tag{2.1}$$

The damping coefficient, γ, may be rewritten in term of the resonator mass, m, the natural resonance frequency, ω_0, and the quality factor, Q, as

$$F = m\ddot{x} + \frac{m\omega_0}{Q}\dot{x} + m\omega_0^2 x. \tag{2.2}$$

The driving force experience by the resonator is electrostatic in nature and arises from the capacitive coupling between the micromechanics and a nearby electrode. The force from this capacitance is found by taking the derivative of the capacitive energy, $U = \frac{1}{2}CV^2$,

$$F = -\frac{dU}{dx} = -\frac{1}{2}V^2\frac{dC}{dx}, \tag{2.3}$$

where the voltage is $V = V_{DC} + V_{AC}e^{i\omega t}$. Combining Equation 2.1 with Equation 2.3 yields

$$F = -\frac{1}{2}\frac{dC}{dx}(V_{DC}^2 + 2V_{DC}V_{AC}e^{i\omega t} + V_{AC}^2 e^{2i\omega t}). \tag{2.4}$$

Equation 2.4 may be simplified by ignoring the time-invariant component of the force and the component of the force entering at twice the AC drive frequency, namely the first and last terms, producing the effective force experienced by the micromechanics upon application of static and alternating fields:

$$F_{effective} = -\frac{dC}{dx}V_{DC}V_{AC}e^{i\omega t}. \tag{2.5}$$

Using the definition of capacitance between parallel plates, $C \equiv \frac{\mathsf{Q}}{V} = \frac{\epsilon_0 A}{x}$, where Q is the charge and ϵ_0 is the permittivity of free space, A is the capacitive area, and x is the distance between the micromechanics and the electrode, we note for later reference that

$$\frac{dC}{dx} = -\frac{\epsilon_0 A}{x^2} = -\frac{C}{x} \quad \& \quad \frac{d^2C}{dx^2} = \frac{2\epsilon_0 A}{x^3} = \frac{2C}{x^2}.$$

2.2.2 Amplitude and Current

From Equations 2.2 and 2.5 the amplitude of oscillation of the resonator may be derived. Setting these forces equal,

$$-\frac{dC}{dx}V_{DC}V_{AC}e^{i\omega t} = m\ddot{x} + \frac{m\omega_0}{Q}\dot{x} + m\omega_0^2 x. \tag{2.6}$$

Taking a solution of the form $x = Ae^{i\omega t}$,

$$x = Ae^{i\omega t} \qquad \dot{x} = i\omega Ae^{i\omega t} \qquad \ddot{x} = -\omega^2 Ae^{i\omega t}, \tag{2.7}$$

and plugging into Equation 2.6 yields

$$A = -\frac{1}{m}\frac{\frac{dC}{dx}V_{DC}V_{AC}}{\omega_0^2 - \omega^2 + \frac{i\omega\omega_0}{Q}}, \tag{2.8}$$

or on resonance, when $\omega = \omega_0$,

$$A = \frac{1}{m}\frac{CV_{DC}V_{AC}}{x\frac{i\omega_0^2}{Q}}. \tag{2.9}$$

Beginning with the definition capacitance $C = \frac{\mathsf{Q}}{V}$ (here Q represents the charge and i is the time-varying current),

$$\mathsf{Q} = CV$$

$$\begin{aligned} \dot{\mathsf{Q}} &= C\dot{V} + V\dot{C} \\ &= C\frac{d}{dt}(V_{DC} + V_{AC}e^{i\omega t}) + (V_{DC} + V_{AC}e^{i\omega t})\frac{d}{dt}C \end{aligned}$$

Expanding this,

$$\dot{\mathsf{Q}} = i\omega CV_{AC}e^{i\omega t} + i\omega V_{DC}\frac{dC}{dx}Ae^{i\omega t} + i\omega V_{AC}\frac{dC}{dx}Ae^{2i\omega t} \tag{2.10}$$

As in Section 2.2.1 we drop the doubled frequency term, yielding

$$\mathsf{i} = \dot{\mathsf{Q}} = i\omega e^{i\omega t}(CV_{AC} + AV_{DC}\frac{dC}{dx}) \tag{2.11}$$

Plugging in the amplitude of oscillation, Equation 2.9, into Equation 2.11 yields the complex current,

$$\mathsf{i} = V_{AC}e^{i\omega t}[i\omega C - \frac{1}{m}\frac{(\frac{dC}{dx})^2V_{DC}^2}{\frac{i\omega_0^2}{\omega} + i\omega + \frac{\omega_0}{Q}}]. \tag{2.12}$$

Taking the real part of Equation 2.12 yields

$$\mathsf{i}_{\mathcal{R}} = V_{AC}e^{i\omega t}(\frac{(\frac{dC}{dx})^2V_{DC}^2Q}{m\omega_0}). \tag{2.13}$$

2.2.3 Micromechanical LRC

Comparing the form in Equation 2.13 to Ohm's Law, $\mathsf{v} = \mathsf{i}R$, shows that the bracketed portion is equivalent to the inverse of the resistance. This quantity, known as the motional impedance, R_m, can thus be written:

$$R_m = \frac{m\omega}{Q(\frac{dC}{dx})^2 V_{DC}^2}$$

or since $\frac{dC}{dx} = -\frac{C}{x}$,

$$R_m = \frac{m\omega_0 x^2}{C^2 V_{DC}^2 Q} \tag{2.14}$$

Using the motional impedance the circuit model, the motional capacitance and inductance of the resonator may be derived. The inductance of the resonator may be found from the impedance of an inductor as follows: The complex impedance is given by

$$Z_L = i\omega L$$

and the electrical quality factor of the inductor, Q, which represents the ratio of the real and imaginary impedances, reads

$$Q_L = \frac{\omega_0 L}{R}.$$

Thus using the motional impedance of the resonator as the real impedance of its circuit model equivalent,

$$L_m = \frac{QR_m}{\omega_0} = \frac{Q}{\omega_0}(\frac{m\omega_0 x^2}{C^2 V_{DC}^2 Q})$$

yields the mechanical inductance:

$$L_m = \frac{mx^2}{C^2 V_{DC}^2} \tag{2.15}$$

The circuit model equivalent capacitance can be found similarly. Beginning with the impedance of a capacitor,

$$Z_C = -\frac{i}{\omega C}$$

$$Q_C = R\omega C$$

$$C = \frac{Q}{\omega_0}[\frac{C^2 V_{DC}^2 Q}{m\omega_0 x^2}]$$

yields the mechanical capacitance:

$$C_m = \frac{C^2 V_{DC}^2 Q^2}{m\omega_0 x^2} \tag{2.16}$$

2.3 Impedance Matching to Micromechanics

2.3.1 Calculations and Practice

This approach to capacitive detection can be described as an impedance match between standard test electronics and a system containing electrically active, capacitively coupled resonant micromechanics, for example a string or membrane. A resonant LC circuit (a tank circuit) acts as the impedance matching element between the high-impedance micromechanics and the (typically) 50 Ω test electronics.

Radio frequency signals impinging upon a perfectly impedance-matched system do not reflect energy upstream. Thus, observation of the reflected signal from a swept frequency source reveals a dip in the reflected spectrum at the resonance frequency of the tank circuit.

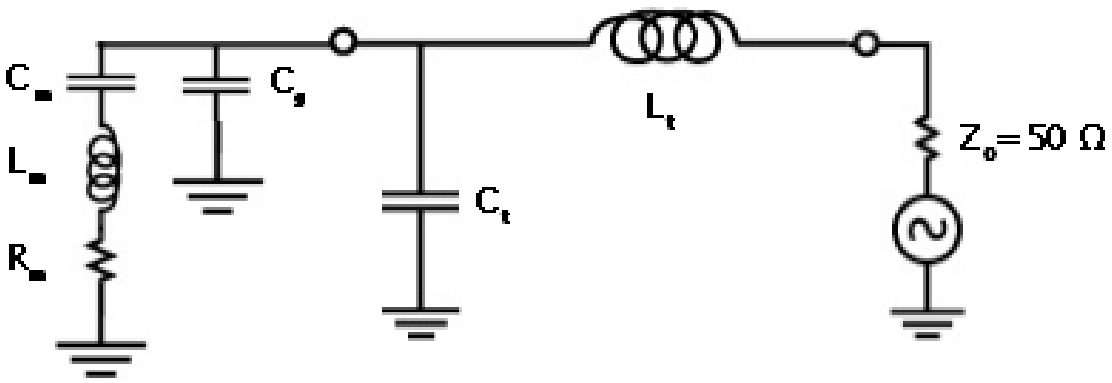

Figure 2.2: Lumped element equivalent circuit. MEMS (L_m, R_m, C_m and gate capacitance C_g) are matched to 50 Ω electonics through an impedance matching tank circuit (L_t and C_t).

In this case, the "system" is composed of the device capacitance, parasitic capacitance, and the impedance of the inductor. (Signals drive the resonating circuit and are in fact lost to the real impedance of the tank inductor as it resonantly exchanges energy with the tank capacitor.) The real part of the inductor impedance often represents the majority of the total system impedance. Thus to a great extent, in order to get the best impedance match (deepest dip in reflected signal) one must primarily impedance match *to the inductor*. The complex impedance of a real inductor is given by a "SPICE" model, as in Appendix C.

Any variation from perfect impedance matching results in a greater reflected signal. The normalized reflection coefficient, Γ, is given by

$$\Gamma = \frac{Z(\omega) - Z_0}{Z(\omega) + Z_0}. \tag{2.17}$$

where $Z_0 = 50\ \Omega$ in most standard test electronics ($Z_0 = 75\ \Omega$ is another standard). In equation 2.17, $Z(\omega)$ is the system impedance as matched by the LC impedance matching network. This transformed system impedance should be made as nearly as possible to match Z_0. In practice equation 2.17 is more conveniently arranged,

$$Z(\omega) = -Z_0 \frac{\Gamma + 1}{\Gamma - 1}. \tag{2.18}$$

The characteristic impedance of a resonant tank circuit matching network is given by $Z_t = \sqrt{\frac{L_t}{C_t}}$, which is equivalent to the geometric mean of the system impedances on either side of the matching network.

$$Z_t = \sqrt{\frac{L_t}{C_t}} = \sqrt{R_m R'_m}. \tag{2.19}$$

Here, R_m is the motional impedance from Equation 2.14 and R'_m is the "transformed motional impedance," the magnitude of the motional impedance as it appears to the 50 Ω electronics on the opposite side of the impedance matching tank circuit. From Equation 2.19 it can be seen that the value of R'_m is set by the values of the components selected. The aim is to *maximize* the value of R'_m.

If we assume a constant gate bias, V_{DC}, $R_m = const.$ Therefor maximization of R'_m can be accomplished by *minimizing* the tank capacitance, C_t and *maximizing* L_t while maintaining the condition $\omega_0 = \sqrt{\frac{1}{L_t C_t}}$.

In practice, two limiting conditions prohibit the realization arbitrarily large values of R'_m. First, the capacitance of the tank circuit cannot be made arbitrarily small. Achieving a capacitance of under 3pF requires careful layout and assembly of the system. This is especially true if a trimmer capacitor is used for tuning the tank circuit (as in Section 2.3.4) since the minimum capacitance of the trimmer is often on the order of 1 pF. Parasitic capacitances from wire bonds, packaging, and solder joints commonly add an additional 1–3 pF. The latter parasitics have been mitigated by designing a printed circuit board that accepts the sample chip directly, obviating the chip carrier.[2] In principle, C_t could be comprised of only the

[2] An issue here is that it is difficult to wirbond to the solder pads of the printed circuit board. This can be overcome by using a small lump of indium metal as a conductive putty, or removing the solder pads by mechanical means (razor blade) and wirebonding to the underlying copper.

parasitic capacitance if a well-engineered tank circuit were not to require tuning.

The second practical limitation to arbitrarily large values of R'_m relates to the real part of the complex impedance of the inductors, $\mathbb{R}(Z_L)$, as in Appendix C. For large values of L_t $^{and}/_{or}$ high frequencies, $\mathbb{R}(Z_L)$ can exceed 50 Ω. Because $\mathbb{R}(Z_L)$ cannot be eliminated, when $\mathbb{R}(Z_L) \gg 50\ \Omega$ good impedance matching is not possible. The investigator must refer to the specifications of specific inductors.

In Figure 2.1 it can be seen that when the micromechanical element is not resonantly driven—when the L_m and C_m are not on resonance they behave as an open circuit, the capacitor impeding low frequencies and the inductor blocking high frequency signals—it effectively plays no role in the system. On resonance L_m and C_m effectively vanish, opening this path to ground and introducing the motional impedance, R_m, to the circuit, adding the value of R'_m to the system. This transformed motional impedance (found with Equation 2.19) disrupts the impedance match at the mechanical resonance frequency, causing the impinging signal to be reflected to a different extent. This difference in reflection coefficient at the mechanical resonance frequency constitutes the signal. An impedance-matched circuit disrupted by micromechanics is depicted in Figure 2.3.

Note: Assuming the system impedance is dominated by the rea part of thel inductor impedance, R_L, as per the SPICE mode, Appendix C, if $R_L > 50\Omega$, the addition of R'_m to the to the system impedance, $Z(\omega)$, will result in a *peak*. Conversely if $R_L < 50\Omega$, the addition of R'_m will result in a *dip* since the addition of R'_m brings $Z(\omega)$ closer to 50ω, *i.e.* closer to $\Gamma = 0$.

2.3.2 Electrostatic Spring Constant

Frequency tuning of the resonator can to some degree be accomplished through application of DC bias. In very soft devices the electrostatic force can tension the

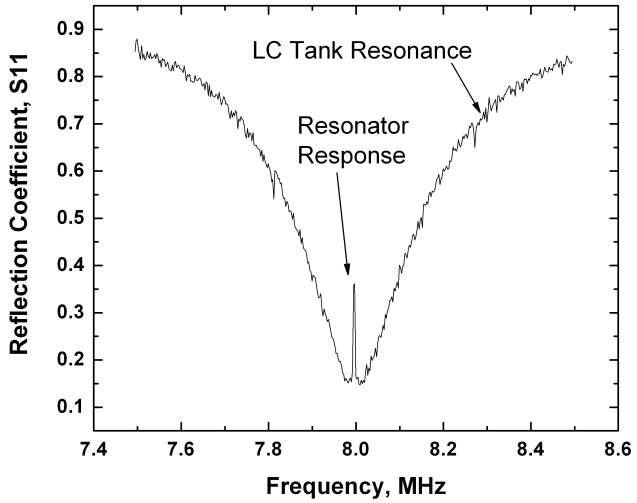

Figure 2.3: Motional impedance of resonant micromechanics disrupts an impedance-matched LC tank circuit resulting in a reflected signal.

resonator, increasing its resonance frequency, but in the case of strong coupling a decrease in frequency with DC bias is observed.

The energy stored in the resonator can be written

$$\varepsilon_{res} = \frac{1}{2}kx^2 + \frac{1}{2}C_g V^2 \tag{2.20}$$

where C_g is the coupling capacitance of the device that varies with device motion. Taylor expanding C_g around $x = 0$ yields

$$\varepsilon_{res} = \frac{1}{2}kx^2 + \frac{1}{2}V^2(C_g(0) + x\frac{\partial C_g}{\partial x} + x^2\frac{1}{2}\frac{\partial^2 C_g}{\partial x^2}) \tag{2.21}$$

where the fourth term is the electrical spring constant,

$$k_e = \frac{1}{2}\frac{\partial^2 C_g}{\partial x^2}V^2, \tag{2.22}$$

or for quick evaluation, $k_e = \frac{CV^2}{x^2}$.

The frequency shift is then given by addition of the mechanical and electrical spring constants, $\omega = \sqrt{\frac{k_m + k_e}{m}}$, which Taylor expands to

$$\omega = \omega_0(1 + \frac{1}{2}\frac{k_e}{k}). \tag{2.23}$$

However, since C_g scales as $1/x$, the second derivative, $\frac{\partial^2 C_g}{\partial x^2}$, will be *negative*, and the frequency will *decrease* with applied DC bias. This downward curvature of the energy potential (going to negative infinity as the resonator approaches the electrode) sums with the upward curvature of the (larger) mechanical harmonic energy potential. The broadens the potential well in the direction of the electrode, decreasing the resonance frequency. If the electrostatic energy increases too much, the potential well will flatten (on the electrode side) and the resonator will "snap in." Note that the equilibrium position of the resonator is not actually required to move closer to the electrode. The small actual shift in the minimum potential can be calculated from the electrostatic force, the capacitance, and the Young's modulus of a given device.

2.3.3 Examples

Example #1: Estimates of R'_m and Initial Circuit

This example demonstrates how to find motional impedance of 35μm-diameter circular membrane, a "drum" resonator. (The resonance frequency of the mechanics is determined in advance, estimated by beam- or shell theory [6, 7] or direct measurement using an optical interferometric technique previously established [8].)

Beginning with Equation 2.14, we find a typical value of $R_m \approx 700\ k\Omega$ using the parameters for an example MEMS. Knowing that our total capacitance is limited to a minimum of $C_{total} = 2.7\ pF$, and given a resonance frequency of $f_0 = \frac{\omega}{2\pi} = 12\ MHz$, using $\omega = \sqrt{\frac{1}{L_t C_t}}$ we find the necessary inductor, $L_t = 66\ \mu H$.

From Equation 2.19 we find

$$Z_t = \sqrt{700,000 \times R'_m} = \sqrt{\frac{L_t}{C_t}}$$

$$R'_m = 36\ \Omega$$

In most devices the coupling to the resonator was limited by the parasitic capacitance of the system. In this case, one selects the largest inductor should be selected that resonates with the capacitance (including parasitic capacitance) at the resonance frequency of the mechanics. As seen in Section 2.3.5, in the case of very good coupling (more readily achieved at low R_m (small gap, d)), detection can be limited by thermal motion (or ambient electrical noise) rather than by C_t.

Example #2: Extracting $\mathbf{R_m}$ from Measurements

Once the resonance spectrum of the micromechanics is recorded by this method, the actual value for the motional impedance and the degree of impedance matching may be determined analytically.

As shown in this example, measurements of the reflected signal from the bottom of the tank resonance and the top of the mechanical resonance are sufficient to ascertain the actual motional impedance of the resonator. Refer to the plot in Figure 2.4 and the parameters described in the caption. Reflection measurements with respect to the background reflection level (the level far from the tank dip) are taken at the top of the resonance peak and at the bottom of at the bottom of the tank dip (with the resonance peak tuned aside). Measured values for the shunt capacitance (combined tank, gate and parasitic) and inductance are ascertained in this experiment using a BK Precision 886 LRC Meter.

In this example, the signal at the bottom of the tank resonance and the top of the resonance peak compared to background are:

$$\mathrm{dB_{tank}} = -11.2\ \mathrm{dB} \quad \& \quad \mathrm{dB_{tank+R_m}} = -1.9\ \mathrm{dB}.$$

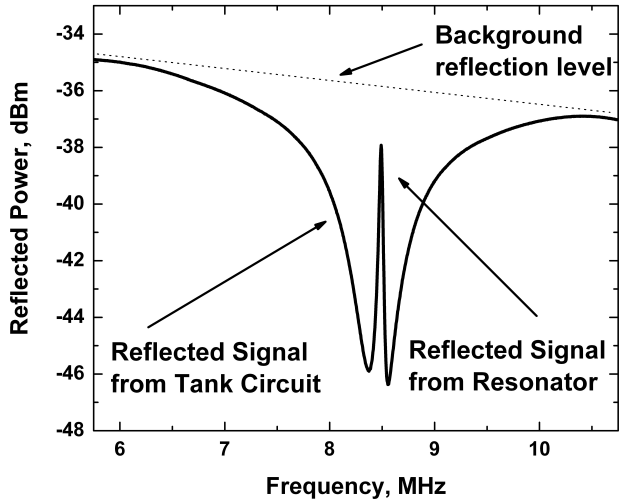

Figure 2.4: Reflectance measurement from a 30 μm-diameter drum membrane with a 223 nm oxide gap and a resonance frequency of 8.45 MHz at $V_{DC} = 10.2V$. An inductor of 44 μH is selected to resonate with the 8 pF capacitance. Q is roughly 1000.

We recall the following relationship for power and voltage given in decibels:

$$\mathrm{dB_{power}} = 10\log(\frac{\mathrm{P_{out}}}{\mathrm{P_{in}}}) = 20\log(\frac{\mathrm{V_{out}}}{\mathrm{V_{in}}}) = 20\log\Gamma \quad \text{Or} \quad \Gamma = 10^{\frac{\mathrm{dB}}{20}},$$

thus,

$$\Gamma_{tank} = 10^{\frac{-11.2}{20}} = 0.28 \quad \& \quad \Gamma_{tank+R_m} = 10^{\frac{-1.9}{20}} = 0.80.$$

The impedance of the tank circuit, as seen from in this case using a spectrum analyzer in conjunction with a directional coupler, is then found using Equation 2.18:

$$Z'_{tank} = -50[\frac{\Gamma_{tank}+1}{\Gamma_{tank}-1}] = 88\ \Omega \quad \& \quad Z'_{tank+R_m} = -50[\frac{\Gamma_{tank+R_m}+1}{\Gamma_{tank+R_m}-1}] = 460\ \Omega \tag{2.24}$$

Taking the difference yields the effective difference in the matching between the tank circuit and the tank circuit including the mechanical resonance: $\Delta Z =$

Table 2.1: Graphene Parameters

$d = 285 \times 10^{-9}$ m	Oxide (gap) distance
$\rho = 2250$ kg/m^3	Density of carbon
$w = 3 \times 10^{-6}$ m	Width of resonator
$l = 5 \times 10^{-6}$ m	Length of resonator
$t = \times 10^{-9}$ m	Thickness of resonator
$m = w \times l \times t \times \rho$	Mass of device
$f_0 = \frac{\omega_0}{2\pi} = 23.3$ MHz	Resonance frequency
$Q = 100$	Quality factor
$V_{DC} = 6$ V	Applied Bias

372 Ω. The 50 Ω test electronics have been matched to a 88 Ω system (rather than the target 50 Ω), and on resonance the micromechanics adds an additional $R'_m = 372$ Ω of impedance. Using Equation 2.19 in reverse yields the actual value for the resonator motional impedance in the system:

$$R_m = \frac{L/C}{372} = 14.7\ k\Omega.$$

Example #3: Detection of Graphene

This example estimates the magnitude of response we expected to see for a reflectance measurement of graphene resonance using the probes described in Section 2.4.2. The devices are graphene resonators suspended between gold electrodes over a vacuum gap. The device parameters are given in Table 2.1.

Plugging the parameters from Table 2.1 into Equation 2.14 we find the motional impedance $R_m = 1.1\ M\Omega$. Using the known (directly measured) inductance $L_t = 15.4\ \mu H$ and the frequency of the tank we find $C_t = 3.0\ pF$, and measure that

half of this capacitance comes from the bond pad. Plugging these values into Equation 2.19 and solving we find $R'_m = 5\ \Omega$.

We measure the reflection of the tank to be 11.0 dB below the background level, and thus find the reflection coefficient $\Gamma = 10^{\frac{-11}{20}} = 0.282$.

Plugging this Γ_{tank} into Equation 2.18 and letting $Z(\omega) = 50\ \Omega$ we find

$$Z(\omega) = -Z_0 \frac{\Gamma + 1}{\Gamma - 1} = -50 \frac{0.282 + 1}{0.282 - 1} = 89\ \Omega, \tag{2.25}$$

which, again, should be to a great extent from $\mathbb{R}(Z_L)$.

We then estimate the reflection from the resonator using Equation 2.17

$$\Gamma_{resonator} = \frac{Z(\omega) + R'_m - Z_0}{Z(\omega) + R'_m + Z_0} = \frac{(89 + 5) - 50}{(89 + 5) + 50} = 0.306. \tag{2.26}$$

The difference in the reflection coefficients is then $\Delta\Gamma = 0.024$, or $\frac{0.024}{1-0.282} = 0.03$ or 3% of the depth of the tank resonance, *i.e.* the peak should be roughly 3% of the tank response. Compared to the tank dip, this is a one-part-in-30 response magnitude. Although not successfully demonstrated, this estimation indicates that detection of graphene resonance by reflection measurement is within the realm of possibility.

2.3.4 Experimental Setup

Large capacitive area and a thin dielectric layer (vacuum) facilitate the capacitive coupling for the electrical detection of micromechanical resonance described in this manuscript. For this reason a membrane geometry was chosen. An exemplary device is depicted in Figure 2.5.

Devices were fabricated at the Cornell Nanofabrication Facility (CNF) from polycrystalline silicon using top-down surface micromachining. Drums were fabricated by etching an orifice in the device layer to expose the underlying silicon

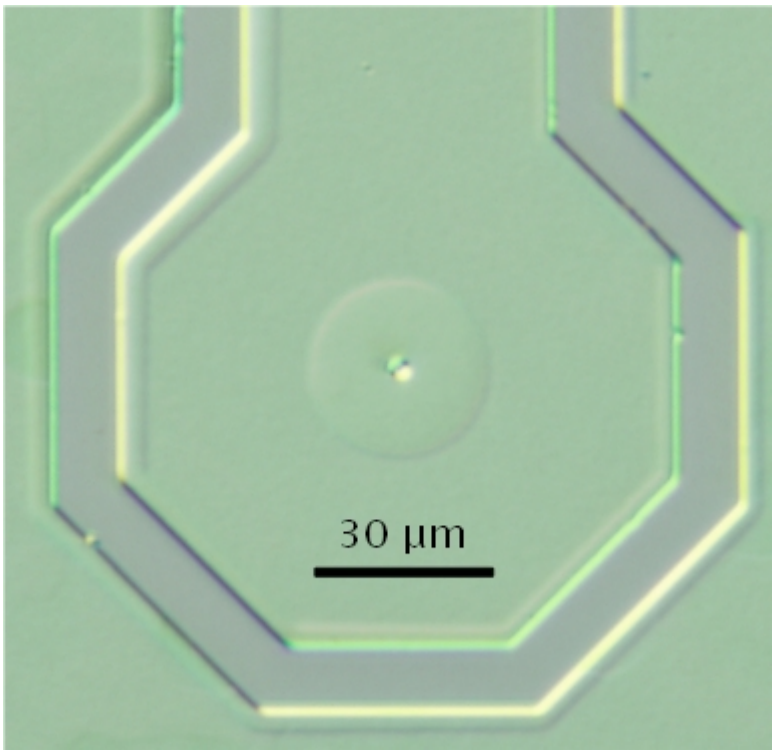

Figure 2.5: Doped polycrystalline silicon drum membrane (circle, center) and the associated bond pad are electrically isolated by a trench excavated through the device layer.

dioxide, and released by means of a wet etch in hydrofluoric acid or an analog. For details of fabrication please refer to Section A.1.

Devices are wirebonded into standard Kyocera ceramic duel in-line packages (DIPs) in order to interface with a custom printed circuit board (PCB). The PCBs for this project were fabricated by Advance Circuits, Inc. The circuit board design and final product are shown in Figure 2.6.

A network analyzer (Agilent 8753ES) was used in reflectance mode (S11) for driving the micromechanics and detecting their resonance. Alternately a spectrum analyzer (Agilent 4402) was used in conjunction with a directional coupler. The drive signal passes through a bias-T where a DC voltage on the order of 5-20V is added to the signal. This DC voltage is not only a primary factor in the signal

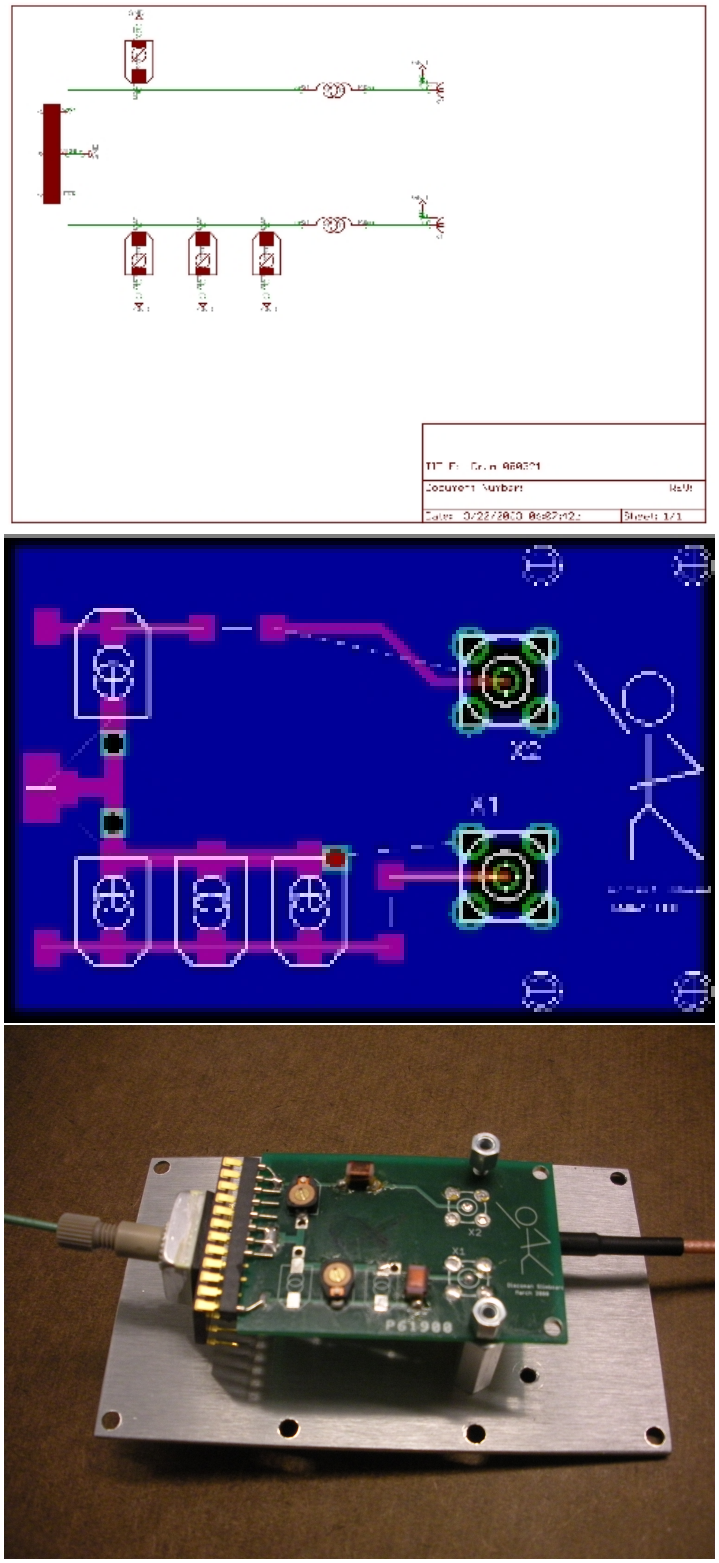

Figure 2.6: Top: Logical schematic, Center: Layout, Bottom: Stuffed impedance matching board. Vacuum line and vacuum cap interface with a standard Kyocera chip carrier, left.

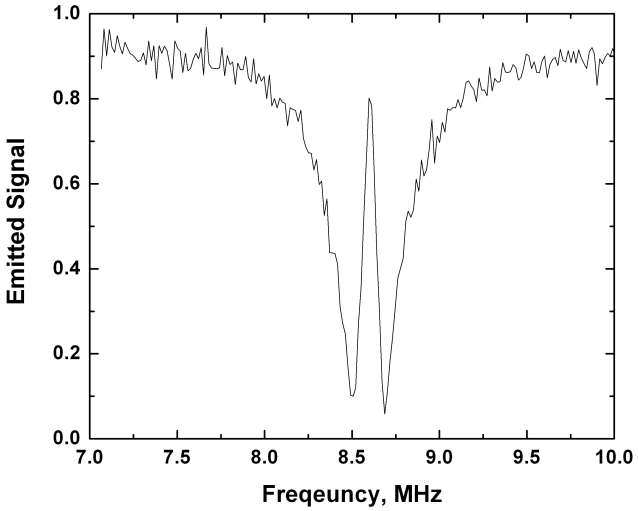

Figure 2.7: "Undriven" motion of a ∼30 μm-diameter tensile polycrystalline silicon drum resonator over a 95 nm vacuum gap. Data averaged over 50 sweeps. Drive power lead is turned off and disconnected. System driven by ambient noise. The bias is 12 V_{DC}.

amplitude, as in shown in Equation 2.9, but also serves to tune the resonance frequency (Section 2.3.2) and motional impedance of the resonator (Equation 2.14).

2.3.5 Limits of Detection

Using the experimental setup described in Section 2.3.4 we are able to detect micromechanical resonance down to nearly the thermal level of motion. This corresponds to the drive power being zero or off, however the device is driven by ambient electrical noise. In this demonstration we employ a ∼30μm-diameter tensile polycrystalline silicon drum resonator, 330 nm in thickness over a dielectric air gap of 95 nm.

The "thermal level" of resonance is depicted in Figure 2.7. The reflection coefficient at the bottom of the LC tank was measured to be $\Gamma = -12.6$ dB below

the standard level (away from tank) and corresponds to a transformed system impedance of $Z(\omega) = 87\Omega$. The tip of the resonance peak reflects power at $\Gamma = -1.8$ dB, corresponding to a transformed motional impedance of $R'_m = 880\Omega$. Real-time monitoring of resonance at the thermal level required around one second of signal averaging, or about five sweeps of the spectrum by the network analyzer.

2.4 Further Demonstrations

2.4.1 Mass Sensing

To demonstrate the compatibility of reflectance measurements in sensing applications we construct a simple vacuum chamber consisting on one side of a tungsten filament intertwined with a gold filament—each 0.003"— and on the other gasketed orifice in which the device package sits. The device side is exposed to vacuum, while for convenience the printed circuit board remains at atmosphere.

The device response was monitored in real time as the filament was heated to visible brightness using a variac. During the ∼5s heating cycles the presence of the gold filament on the tungsten filament was apparent since that portion of the filament did not glow as brightly (the thermal energy being employed in the phase transition of the gold). The disappearance of visible cold spots in the filament corresponds to the discontinuation of resonator frequency shifts with subsequent flashes.

Frequency shifts due to the added mass of the gold on the dome resonator surface are depicted in figure 2.9. Assuming small added mass and frequency shift compared to the total mass and frequency of the resonator, the observed frequency shifts and $\frac{\Delta f}{f} = -\frac{1}{2}\frac{\Delta m}{m}$ suggest a total deposited mass of $\Delta m \approx 1pg$. With the apparent peak half-width of ∼12 kHz and assuming $^1/_{10}$-peak-width resolution,

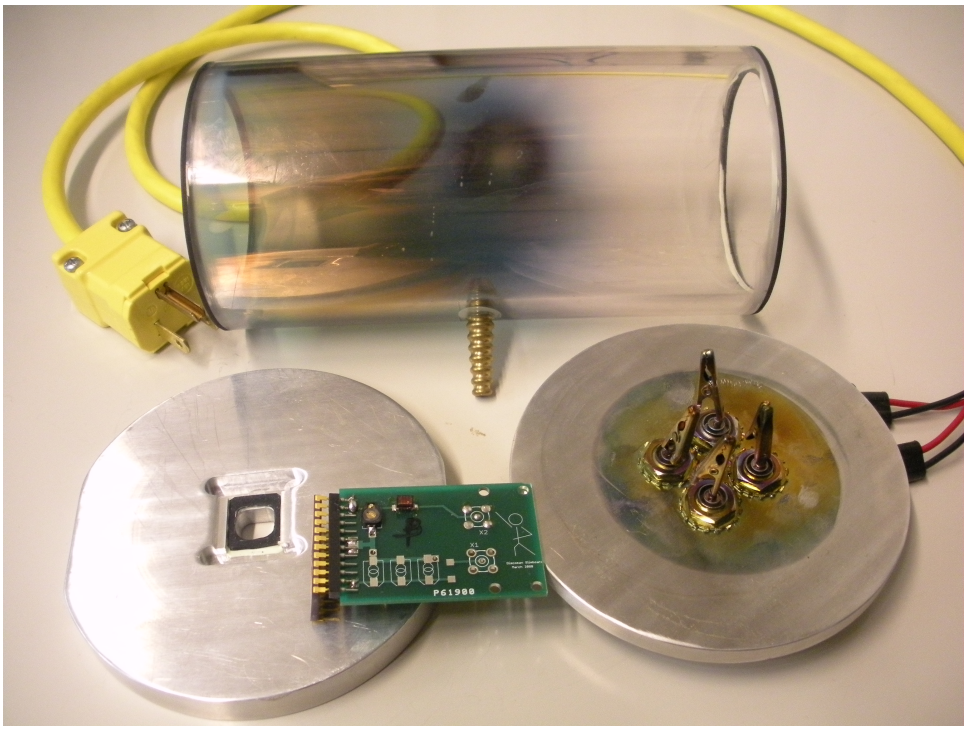

Figure 2.8: Basic demonstration of mass sensing using capacitive detection of a micromechanical dome resonator using a lightbulb-inspired tungsten wire thermal evaporation system.

the mass sensitivity of these sensors is of the order of 1 fg.

2.4.2 LC Probes

An interesting aspect of electrical readout via LC impedance matching is the very simplicity, and thus, potentially its versatility. The requirement of only two circuit elements and a single lead facilitates integration of the readout scheme onto standard probe tips, as depicted in Figure 2.10. Probe-based detection of drum and dome resonance was successfully demonstrated by this method. However, probe-based matching circumvents the need for wire bonds and packaging opens, enabling the address of non-traditional devices. An outstanding example is graphene.

At the time of the experiment graphene fabrication was accomplished by a

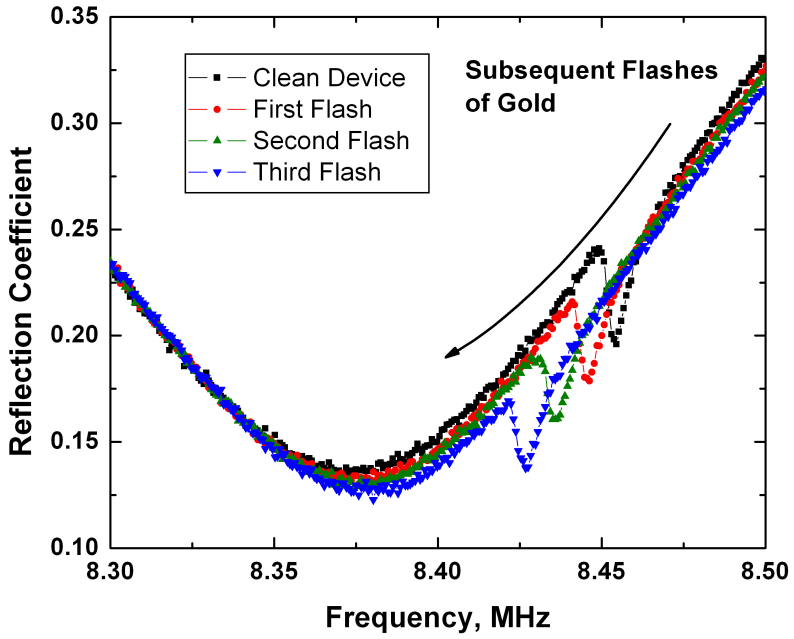

Figure 2.9: Frequency shifts due to adsorption of gold mass onto the surface of a micromechanical dome resonator. Gold is thermally evaporated in sequential rapid heatings of a gold-laden tungsten filament. Resonator response appears as a dip in this case because the impedance matching circuit is "over-matched," *i.e.* the addition of the motional impedance brings the system closer to 50Ω.

mechanical exfoliation method involving high purity Kish graphite and common Scotch tape, and electrical contacts were unavailable. An attempt was made to read out the suspended membranes in Figure 2.11. Devices at that time displayed quality factors $Q < 200$, which poses the difficulty to this readout method that the width of the desired signal peak is on the scale of the detection window. The small area of the devices in combination with roughly 3 pF of parasitic capacitance inherent to the LC probe put detection at the edge of possibility—calculation predicted a roughly 3% change in the depth of the LC reflectance curve. See Example #3, Section —refexample3. Observed, however, was reproducible fluctuation of

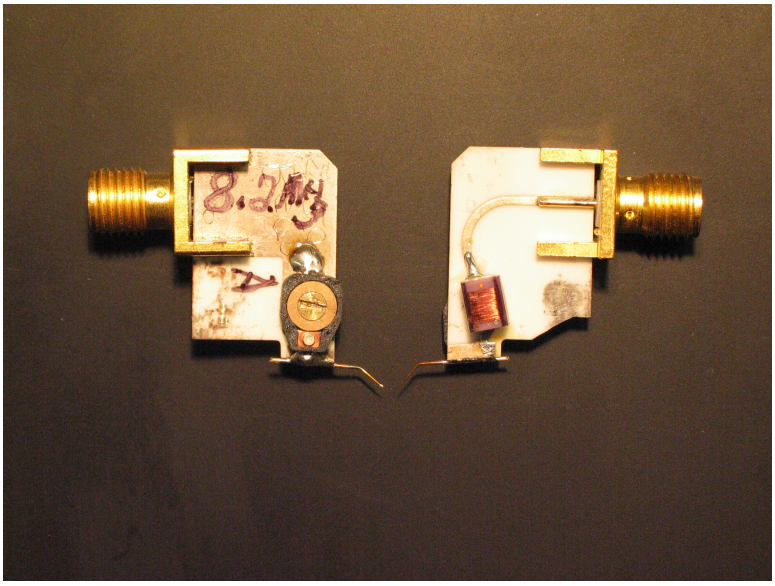

Figure 2.10: Probe-mounted electrical readout circuit.

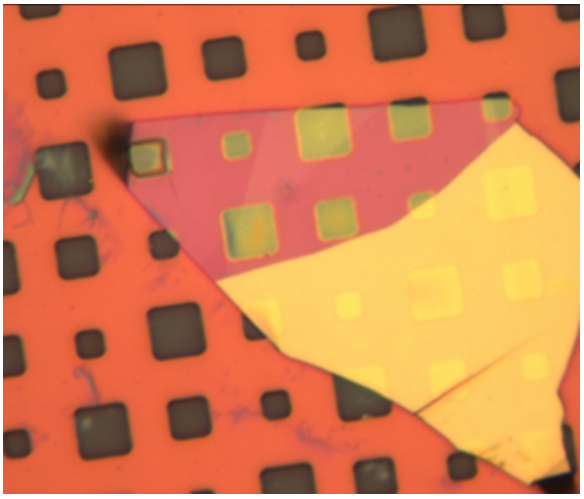

Figure 2.11: Graphene and multi-layer graphene deposited by mechanical exfoliation is suspended above cavities in SiO_2. Credit: Robert Barton

the LC curve at the resonance frequency—known from optical reflectometry—at a specific DC offset. The rigors of making direct electrical contact with the probe tip to the graphene (away from the suspended portion) during the tank tuning caused device failure during an attempted cool down, where it was hoped the increased quality factor would allow direct observation of the resonance peak. Although conclusive results were not recorded, this demonstration illustrates the versatility of the method.

2.4.3 Parametric Amplification

In this section we demonstrate all-electrical parametric amplification of drum resonators. Parametric amplification of micromechanics was demonstrated by Rugar and Grütter [11] in their 1991 *Physical Review Letter*, "Mechanical Parametric Amplification and Thermomechanical Noise Squeezing." In parametric amplification, some parameter of the electromechanical system is modulated with regard to the resonant motion. In the example presented here that parameter is the electrical spring constant, which is modulated by a drive signal at twice the resonant frequency. The phase of this *2f* signal relative to the *1f* drive signal, whose role it is to set the reference phase, controls the resulting mechanical gain.

Parametric amplification confers the particular benefit of preamplification of the resonant mechanical motion before it is ever exposed to the inherent noise of an electrical signal amplifier, thus mitigating the effects of amplifier noise feeding back into the micromechanics.

Rugar and Grütter derive the phase-sensitive gain, $G(\phi)$ of the amplifier:

$$G(\phi) = [\frac{\cos^2\phi}{(1+\frac{V_p}{V_t})^2} + \frac{\sin^2\phi}{(1-\frac{V_p}{V_t})^2}] \tag{2.27}$$

Here, V_t is the threshold voltage at which the pump strength goes to infinity and

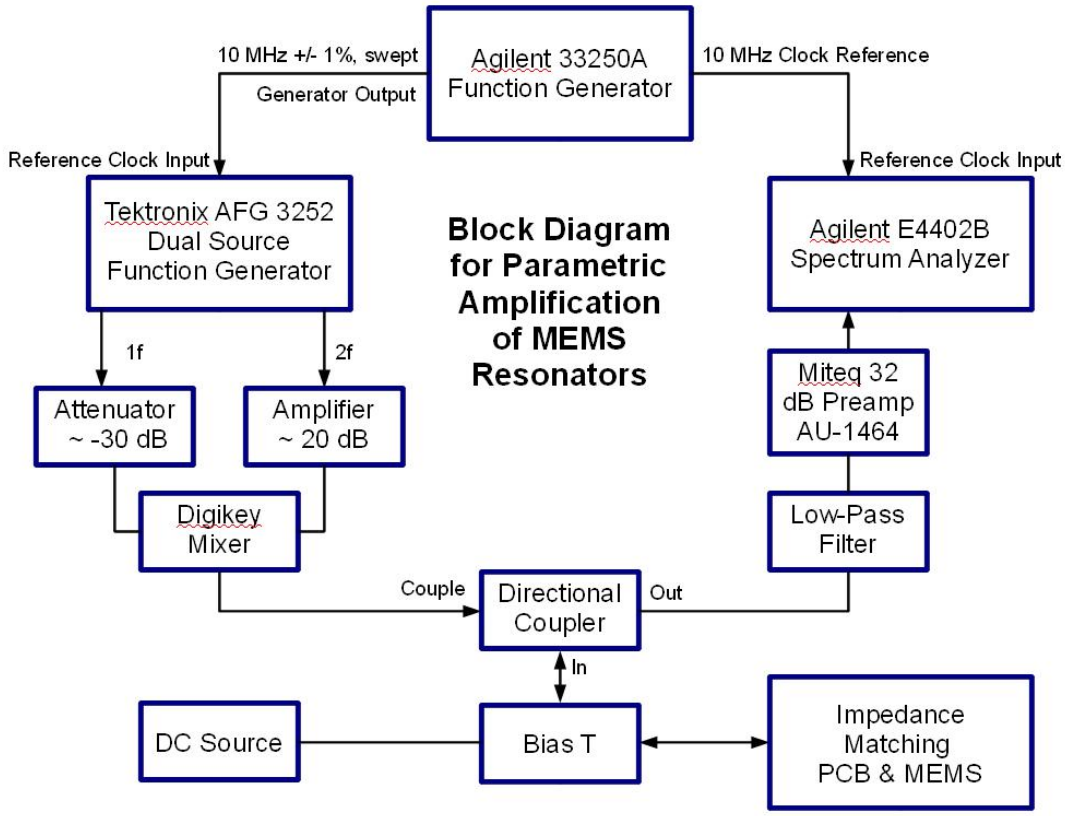

Figure 2.12: Block diagram for all-electrical parametric amplification and readout of micromechanical resonators.

is given by

$$V_t = \frac{2k_0}{QV_0}\left(\frac{\partial^2 C}{\partial x^2}\right) = \frac{4k_0}{QV_0}\frac{C}{d^2}, \tag{2.28}$$

V_p is the *2f* pump voltage amplitude and V_0 is the DC bias voltage. Equation 2.27 illustrates that while one quadrature of motion is amplified, the other is deamplified. It should be noted that the gain is maximized for a phase angle of $\phi = {}^{\pi}/_{2}$ and is in fact negative and is in fact less than unity for $\phi = 0$. The greatest deamplification realizable at $V_p \to V_t$ is $G(\phi = 0) \to \frac{1}{2}$. A block diagram of the setup for parametric amplification is depicted in Figure 2.12. Using a second function

generator to sweep the reference clock of the duel source machine overcomes the difficulty of sweeping the frequency of the *1f* and *2f* signals while maintaining control of their relative phases. Specifically, a duel source function generator produces a pair of single tones of tunable relative phase. A swept signal is generated from these tones by using a third function generator to sweep the 10 MHz reference clock of the duel source function generator.[3] The analyzer is set to the appropriate frequency window and sweep time to synchronously receive the reflected signal. All sweeps are triggered by the clock controller.

Results for parametric amplification in drum resonators are depicted in Figure 2.13 and Figure 2.14, begrudgingly separated into two figures for satisfaction of formatting requirements. Results for drum resonators depict the gain as a function of phase, and as the drive approaches the threshold, Figure 2.15. No distinct narrowing of the resonance is observed.

2.5 Conclusion

The electrical detection scheme for resonant device readout demonstrated in this chapter represents an experimentally useful method of device interrogation. It is the hope of the author that this description will ease the entry to the technique for other graduate students in the field.

As described in the future work, Chapter 6, further benefit may come of continued study of parametric effects. For example, further research should explore the behavior of parametrically amplified oscillators operating in air. (It was the observation of the author that when compared to normally driven (*1f*) drum resonators, parametrically driven devices maintained appreciable signals to higher

[3]The maximum deviation from 10 MHz reference allowed by the generator is 50 kHz, limiting the window for the phase-controlled duel frequency sweeps to 1% of the resonance frequency.

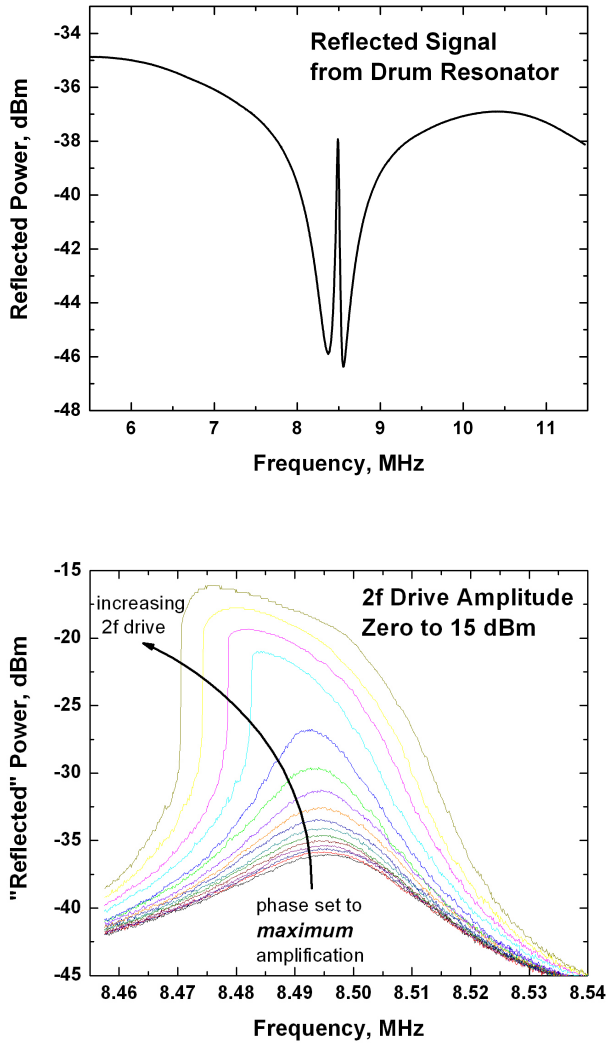

Figure 2.13:

a) Reflected signal from drum resonator: This wide view depicts the resonator signal lodged in the LC tank resonant response. The subsequent data are of the same resonator in the same configuration—same scale bars—but technical details require a window of a particular frequency span for parametric drive in this system. Though out of sight, the level of the wings beyond the LC dip remain at the same level. **b)** Response of resonator at constant phase corresponding to maximum gain with increasing *2f* drive power.

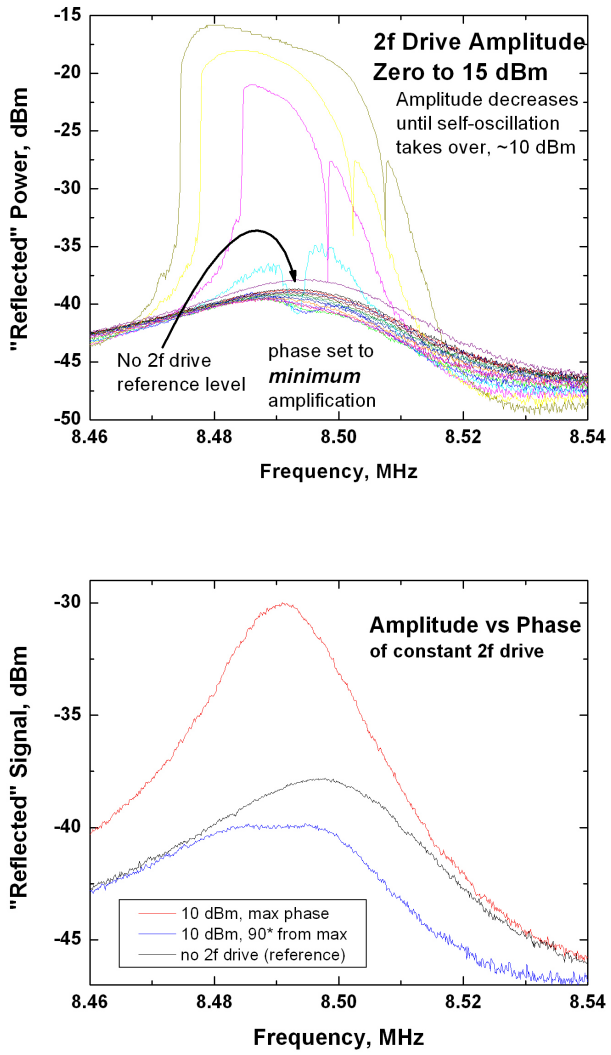

Figure 2.14:

Continuation of Figure 2.13 **c)** Response of resonator at constant phase corresponding to minimum gain ($G < 1$) with increasing *2f* drive power. **d)** Response at constant *2f* drive power set to ~0.9 V_t with the phase set to maximum and minimum gain ($\Delta\phi = 90$). Undriven (no *2f*) peak included for reference. Note that the peak rises well above the level of the tank.

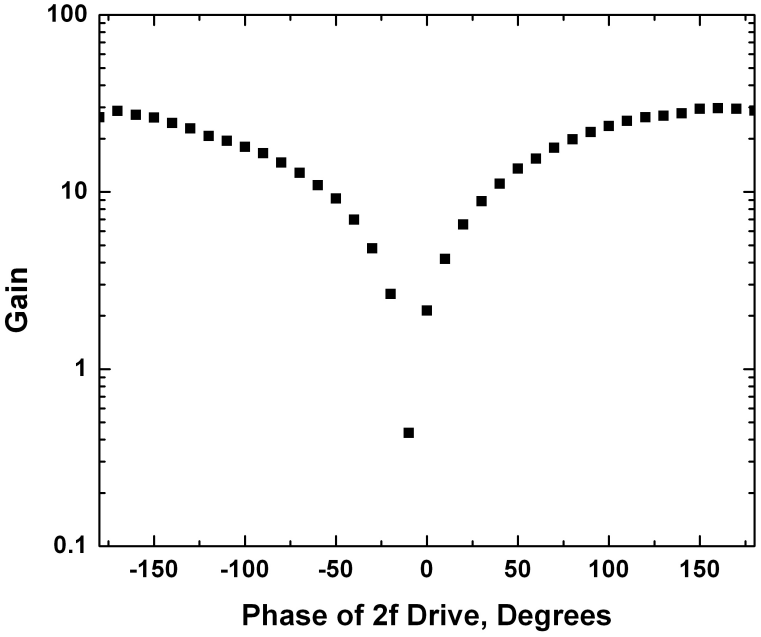

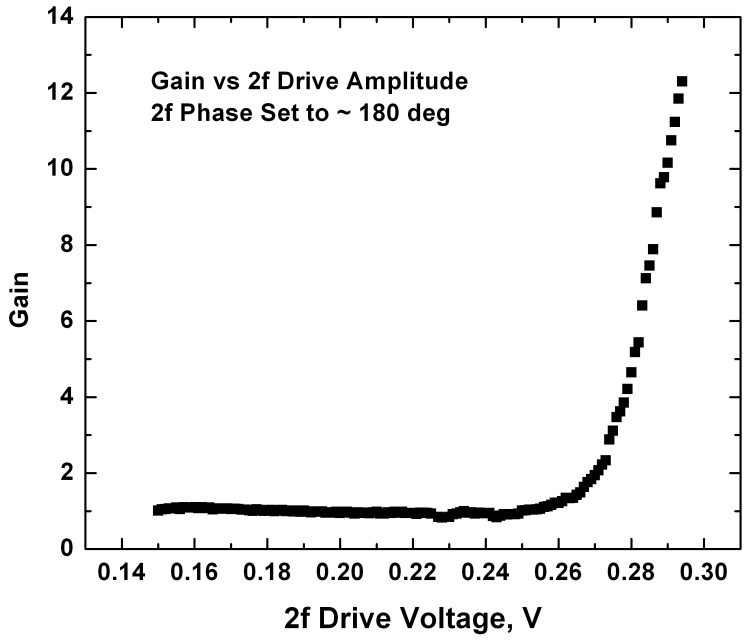

Figure 2.15: **a)** The gain of a dome resonator (different device from Fig. 2.13) as a function of phase using a *2f* drive amplitude near the threshold voltage. **b)** Gain with respect to un-*2f*-driven dome resonator as the *2f* drive amplitude approaches the threshold voltage.

pressures.) If carefully applied, this technique, due to its low power and simple implementation, has the potential to supply a realistic electrical readout scheme for future resonant MEMS sensor technology.

BIBLIOGRAPHY

[1] T. Rocheleau, T. Ndukum, C. Macklin, J. B. Hertzberg, A. A. Clerk, and K. C. Schwab, Nature **463** 7277 72-75 (2010)

[2] A. D. O'Connell, M. Hofheinz, M. Ansmann, R. C. Bialczak, M. Lenander, E. Lucero, M. Neeley, D. Sank, H. Wang, M. Weides, J. Wenner, J. M. Martinis and A. N. Cleland, Nature **464** 697-703

[3] Q. P. Unterreithmeier, T. Faust, S. Manus, and J. P. Kotthaus, Nano Letters **10** 3 887-890

[4] M. Li, H. Tang, M. L. Roukes, Nature Nanotechnology **2** 2 114-120 (2007)

[5] Patrick A. Truitt and Jared B. Hertzberg and C. C. Huang and Kamil L. Ekinci and Keith C. Schwab, Nano Letters **7** 1 120-126 (2007)

[6] S. Timoshenko, *Theory of Plates and Shells*, McGraw-Hill, New York 1940

[7] T. D. Rossing, *Principles of Vibration and Sound*, Springer-Verlag, New York 1995

[8] D. W. Carr and H. G. Craighead, Journal of Vacuum Science & Technology B **15** 6 2760-2763 (1997)

[9] Thesis of Dustin W. Carr, Cornell University 2000

[10] Thesis of Jared B. Hertzberg, University of Maryland, College Park, 2009

[11] D. Rugar and P Grütter, Physical Review Letters **67** 6 699-702

CHAPTER 3

PRESSURE DEPENDANT RESONANCE FREQUENCY OF MICROMECHANICAL RESONATORS

3.1 Abstract

We examine the relationship between squeeze film effects and resonance frequency in drum-type resonators. We find that the resonance frequency increases linearly with pressure as a result of the additional restoring force contribution from compression of gas within the drum cavity. We demonstrate trapping of the gas by squeeze film effects and geometry. The pressure sensitivity is shown to scale inversely with cavity height, and sound radiation is found to be the predominant loss mechanism near and above atmospheric pressure. Drum resonators exhibit linearity and sensitivity suitable to barometry from below ten Torr up to several atmospheres. [1]

3.2 Introduction

Micro- and nanoscale resonant technology shows enormous promise in sensor applications due to their high frequency, low mass, and large surface-to-volume ratio. Detection of extremely small masses has been demonstrated with nanomechanical resonators in vacuum [1, 2] and liquid environments [3]. Force sensors (accelerometers) and scan probe techniques based on resonant MEMS have been developed. In this chapter we describe a linear resonant pressure sensor based on squeeze film effects. In our circular membrane drum resonators, we harness squeeze film ef-

[1] This chapter is based on a manuscript published in Applied Physics Letters and reprinted with permission from Darren R. Southworth, Harold G. Craighead, and Jeevak M. Parpia, "Pressure-dependent resonant frequency of micromechanical drumhead resonators", *Applied Physics Letters* **94** 213506, May 27, 2009. Copyright 2009, American Institute of Physics

fects by using the compressibility of the air film below the drumhead membrane to create a pressure-proportionate addition to the mechanical spring constant. The result is a resonator that displays sensitive and linear frequency response from a few Torr to multiple atmospheres of pressure.

Drum resonators, depicted in Figure 3.2b, inset, are fabricated standard lithographic processes on an SOI wafer. We lithographically define etch orifices in a polysilicon device layer that comprises the drumhead when the underlying oxide layer is removed by wet etch in HF to create the drum cavity. We use a 330 nm-thick n-doped polysilicon device layer grown by low pressure chemical vapor deposition (LPCVD) in conditions resulting in an inherent tensile film stress of 400 MPa; the tensile stress ensures that the membranes are flat, as verified by the absence of Newton rings [4]. Devices in this work move in the out-of-plane direction and are driven and detected optically [5], but have demonstrated compatibility with piezo buzzer drive and both electrical drive and detection by the technique described in Chapter 2. Details of the film preparation can be found in Section A.2.

We investigate the pressure sensitivity of the resonant frequency to the variation in the cavity height by considering three identical drum geometries (28 μm diameter, 4 μm etch orifice). The drums exhibit vacuum frequencies 9.38 $\pm$ 0.15 MHz and vacuum quality factors, $Q \approx 1.4 \times 10^4$, and differ only in their respective cavity heights of 95, 235, and 660 nm. The mechanical spring, k, constant of the membranes is found by $k = \omega^2 m_{eff}$ to be $\sim$1500 N/m, where $\omega = 2\pi f$ and f is the resonance frequency of the fundamental mode. The mass of the resonator is taken to be the membrane volume times its density. The effective mass will be smaller by a mode-dependent geometric factor arising from non-uniform motion of the surface.

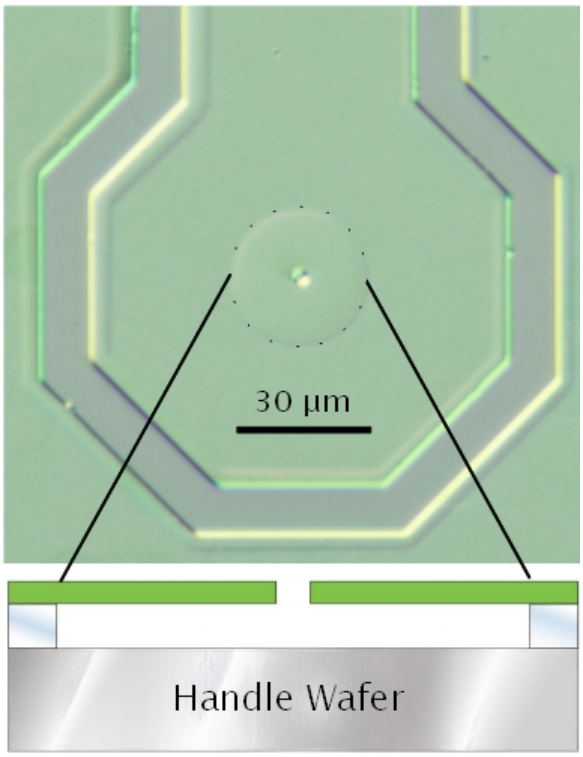

Figure 3.1: Drum and from above and in profile. Doped polycrystalline silicon drum membrane (circle, center) and the associated bond pad are electrically isolated by a trench excavated through the device layer. The trench surrounding the drum also encircles a bond pad. Cartoon not to scale.

3.3 Theory

It has long been observed [6, 7, 8] that microresonators operating in gas while in close proximity to a substrate experience damping due to compression, or squeezing, of the gas film. This arrangement, ubiquitous in MEMS applications, is especially relevant to the plate-like geometries and narrow air gaps associated with capacitive sensing and electrical drive, and squeeze film effects play a significant role in the design of microtorsional mirrors [9] and accelerometers [10]. The effects of squeeze film damping are still under investigation [30, 12, 13], most often in the context of mechanical energy loss mechanisms. Squeeze film damping exhibits

two distinct regimes, referred to by Bao [30] as the viscous and elastic damping regimes. In the first, dominant at lower frequencies and large gaps, the resonant motion of the device forces gas to flow from or toward the compressed volume. In the elastic, or high frequency regime, gas beneath the vibrating structure cannot flow a significant distance within the period of an oscillation and is compressed between the device and the substrate. A gas film trapped by elastic damping does not cause dissipation in the resonator due to viscous flow. However, the increased pressure beneath the device membrane contributes an additional restoring force, increasing the effective spring constant and the resonant frequency.

The viscous damping force and the elastic restoring force have equal magnitude at the cut-off frequency, ω_c, described by Griffin et al. [6] to be,

$$\omega_c = \frac{\pi^2 d^2 P_a}{12 \mu a^2} \tag{3.1}$$

where d is the distance between the substrate and the vibrating surface, P_a is the ambient pressure, μ is the viscosity of air, and a is the typical dimension of the microstructure: the width or length in the case of rectangular geometries or radius in circular geometries (the narrowest dimension is most relevant). Previous research by Andrews et al. [14, 15] has explored the regime above the cut-off frequency. Their devices displayed a quadratic frequency dependence on pressure above 10 Torr because above that pressure the $\omega_c > \omega_0$. Below that pressure, however, the gas spring constant, k_g, was small compared to the mechanical spring constant and resulted in linear frequency shifts with pressure. In this Chapter, we demonstrate operation at frequencies $\omega \gg \omega_c$ and gas spring constant that is small compared to the mechanical spring constant over the relevant pressure range of 10 Torr to atmosphere (by a factor of three at atmospheric pressure for our largest-gap device). In these conditions, drum resonators reside in a regime where the resonant frequency is linear with pressure variation (over the range of mTorr

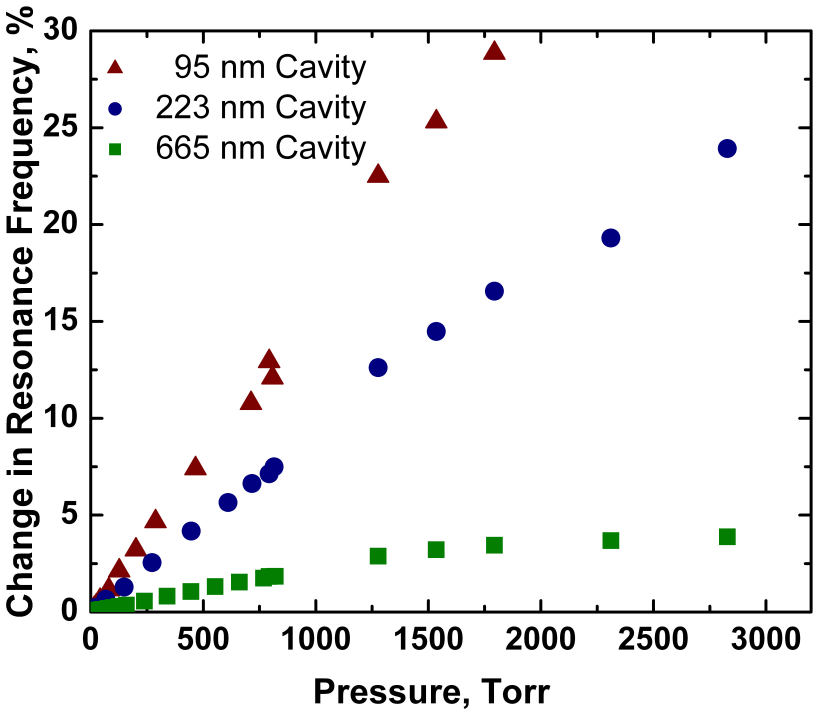

Figure 3.2: Drum resonators' frequency increases linearly with pressure from $\sim$ 1 Torr to $\sim$ 4 atmospheres. The pressure sensitivity varies inversely with cavity height for a drum with 4 μm etch orifice diameter. Gas in the 665 nm-cavity device becomes unclamped above 1 atmosphere, that is, the viscous penetration depth, $\delta = \sqrt{\frac{2\eta}{\rho\omega}}$, is smaller than the gap at pressures above 800 Torr. Here, $\eta = 1.98 \times 10^{-5}$ Pa s is the pressure-independent viscosity of air, and $rho_{air} = 1.2$ kg/m^3.

to several atmosphere for our narrower-gap devices). This development facilitates the operation of resonant pressure sensors at and above atmospheric pressures.

Figure 3.2a shows the variation of frequency change with pressure for three cavity heights. As the pressure is varied, we observe a linear increase in resonant frequency from the low Torr range to several atmospheres, and a fractional frequency shift with pressure, $\frac{\Delta f/f}{\Delta P_a}$, that is inversely proportional to the cavity height.

Previous work by Andrews et al. [15] demonstrated that the squeeze film is compressed isothermally, signifying the equation of state for the gas $pV = const.$ Blech [8] obtains a dimensionless squeeze number for isothermal compression, σ, given by the expression

$$\sigma = \frac{12\mu a^2 \omega}{P_a d^2} \tag{3.2}$$

Low squeeze numbers indicate that the gas will readily flow from the compressed area during an oscillatory period; high values indicate that the gas is trapped, clamped by its viscosity. Our resonators have σ of 3000, 550, and 60 at atmospheric pressure for the 95, 223, and 665 nm -gap devices, respectively, where the elastic regime presides above $\sigma = \pi^2$. In the limit of such large σ the isothermal spring constant of the gas, k_g, formulated by Blech [8] reduces to

$$k_g = \frac{P_a A}{d} \tag{3.3}$$

where A is the plate area. For small changes in spring constant, k_g, and small amplitude Δd, we make the approximations,

$$\Delta f = \frac{1}{2} f(\frac{\Delta k}{k})$$

and

$$\Delta k = \frac{dF}{dx}$$

from which

$$\Delta f = \frac{f}{2}(\frac{AP}{kd}). \tag{3.4}$$

3.4 Experimental Setup

A simplified schematic of the pressure control, optical and electrical systems are shown in Figure 3.3.

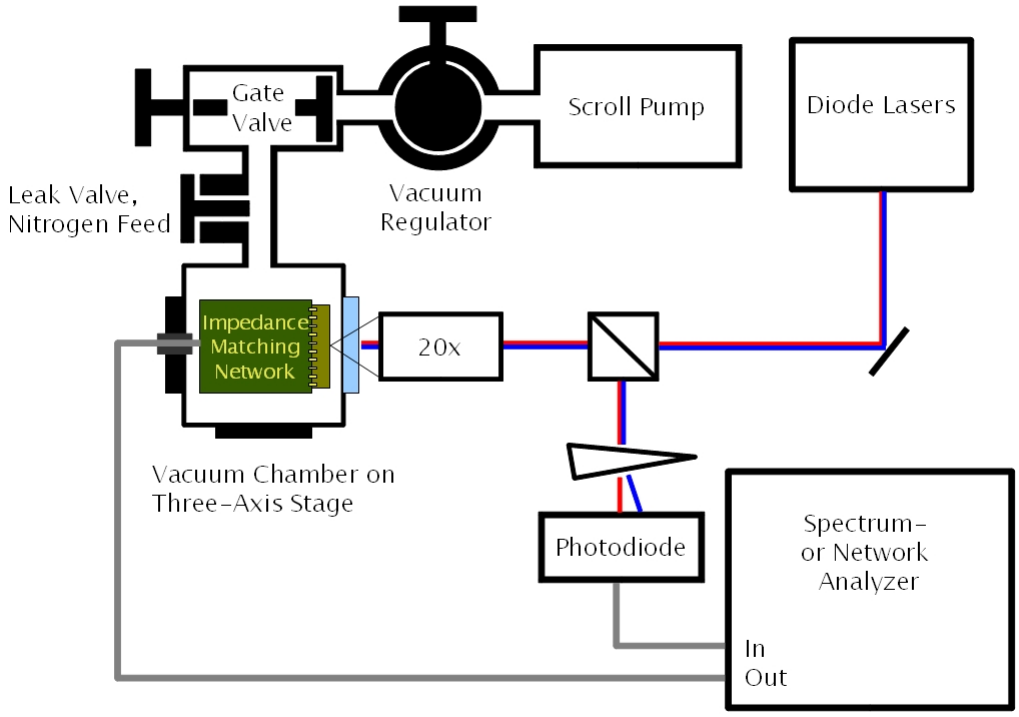

Figure 3.3: Simplified schematic of pressure setup. Sub-atmospheric pressures are controlled by a MKS 600 Series pressure regulator that operates as a throttle between a gas leak and a vacuum pump. Extra-atmospheric pressures are controlled by a nitrogen tank regulator and monitored with a mechanical gauge. The readout can be configured for simultaneous drive/detect by optical and electrical schemes. In the optical scheme, drive (blue) and detection (red) lasers are focused onto the resonator. The intensity of the light reflected from the device and its underlying substrate is modulated by the Fabry-Pérot effect and read out by the photodetector (blue light is diverted). The electrical scheme is described in Chapter 2. Not shown in figure: Camera for positioning, white light source, and polarizers which are used in conjunction with the polarizing beam splitter to maximize reflected signal to the photodiode.

The setup is differently configured for pressure control above and below ambient. For pressure control below one atmosphere, nitrogen (or air) is leaked into the system from an inlet valve in the vacuum line immediately outside the vacuum chamber. The device is arranged facing away from the gas inlet. Pressure is reproducibly regulated by an automated throttle valve downstream of the inlet: an MKS 600 Series PID-controlled butterfly valve with an associated up-stream pressure sensor. The pressure regulator system is unstable at pressures below 500 mTorr and manual throttling with the gate valve is necessary.

For high pressure operation, the vacuum line is closed and nitrogen is introduced at pressure controlled by the regulator. A dial pressure gauge installed on a vacuum flange is used for pressure readout. The standard vacuum window is replaced with a $^1/_2$" clear plastic flange with an o-ring seal.

For electrical contact devices are wire bonded into standard 24-pin Kyocera ceramic DIP packages. Packages are arranged facing the window of the vacuum chamber to allow access to the optical system. Custom-fitted printed circuit boards (see Section 2.3.4) that interface with SMA feedthroughs on the opposite flange account for placement. Printed circuit boards are shorted when only electrostatic drive (without detection) is desired. The trimmer capacitor of the impedance matching circuitry for electrical detection must be adjusted at atmosphere, but can be accessed through the top flange of the chamber. Simultaneous electrical and optical assay can be accomplished by committing the network analyzer (AG8753E) to the electrical system, using the spectrum analyzer (AG4402B) only as an input for the photodiode (no drive), and aligning the frequency spans, sweep times and trigger timing of the two machines. Electrical drive and detection (Section 2.3) was not possible above 500 Torr due to small signal amplitudes and signal peak widths comparable to the detection window.

The optical system is standard practice within the group and is described in detail elsewhere [16].

3.5 Results

We find that our measured squeeze film contribution in Figure 3.2 matches theoretical estimation for k_g at atmosphere to within 20%, the disparity most likely arising because the displacement of the drum, Δd, is not uniform across the entire surface, and thus the actual change in volume, $\Delta V = A\Delta d$, is an overestimate. The frequency dependence on temperature in drum resonators is small compared to pressure-induced frequency shifts; $\Delta f/\Delta T$ is found to be -44 $^{Hz}/_{\circ C}$ over the range of 20 to 250 °C, measured in a Linkam temperature-controlled stage under vacuum. No frequency dependence is found for different amplitudes of motion.

Significant earlier effort has focused on the effect of edges and holes on squeeze film damping. Edge effects at the periphery may be neglected for drum-type resonators since those borders are closed. However, at the central orifice we find both the maximum amplitude of oscillation in the fundamental mode in which our sensors operate, and the sole egress from the cavity. Although the pressure variation is expected to drop exponentially at the borders of a squeeze film, simulations by Veijola [17] limit these border effects to roughly 1.3 times the cavity height, or less than $1\mu m$ in all of our devices. We observe invariance of the dissipation ($\frac{1}{Q}$) and absolute frequency shift to orifice dimension, Figures 3.4. Thus the effect of the etch orifice is tantamount to a negligible loss of compression area. As long as the orifice is significantly larger than the cavity height, its dimension is irrelevant, and a drum resonator may be tailored to a desired pressure sensitivity and operating range entirely by varying the etch time (area) and oxide thickness of the device.

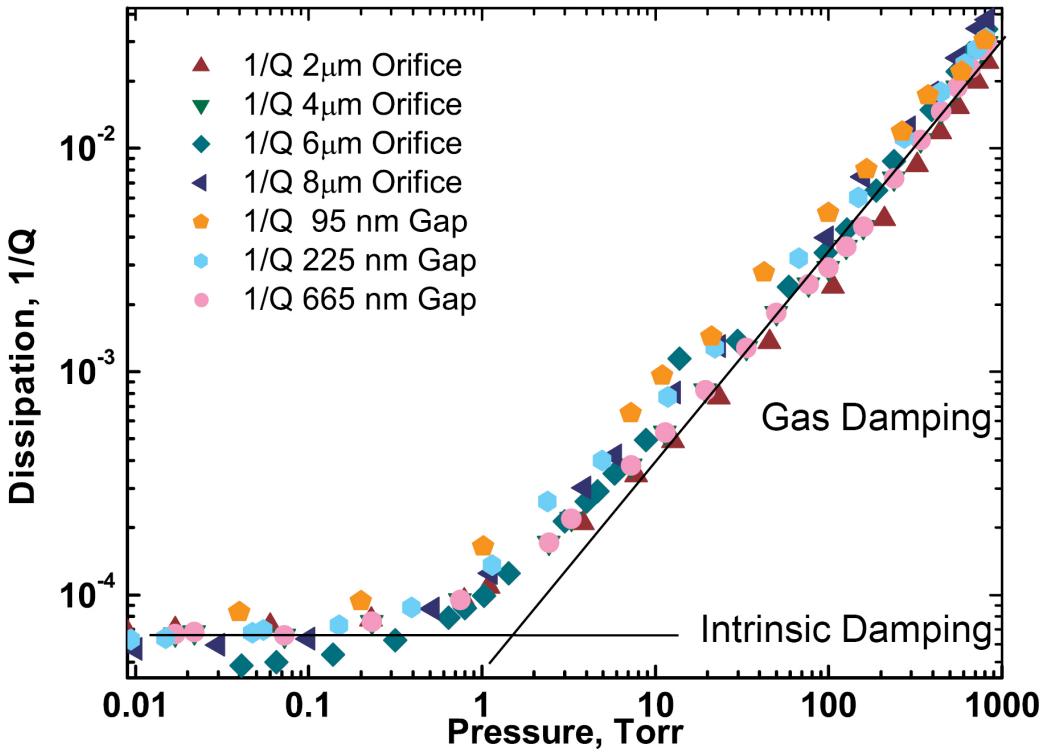

Figure 3.4: Dissipation ($\frac{1}{Q}$) in drum resonators in air is independent of cavity height or orifice size.

3.6 Discussion

Above one Torr, gas damping overwhelms the intrinsic, material (or geometry) -dependent losses observed at lower pressures [30, 13, 18]. Gas within the drum cavity is elastically clamped, leaving acoustic radiation from the upper surface as the primary energy dissipation mechanism. This suggests that heightened Q in air could be obtained by creating a comparably small cavity on the top side of the resonator. See further consideration in future work, Chapter 6.

Figure 3.4a shows the departure of the dissipation from the low pressure, low loss regime to a regime where the dissipation, $\frac{1}{Q}$, increases linearly with pressure.

The expected energy loss to sound radiation can be estimated by considering

the sound radiation from a sphere [19]. The power, p, radiated by a sphere is given by

$$p = 2\pi\rho c R^2 |u^2|, \tag{3.5}$$

where R is the sphere radius, $|u^2|$ is the velocity, and the energy loss per cycle is then $\frac{\Delta E}{cycle} = \frac{p}{f}$. Dividing the total power radiated by the area of the sphere in Equation 3.5 yields the per-area power emanated. Multiplying this by the resonator surface area yields

$$p_a = \frac{1}{2}\rho c |u^2| \pi a^2 \tag{3.6}$$

where a is the drum radius. Then starting from the definition

$$Q = \frac{E}{\Delta E} = \frac{\frac{1}{2}\rho_{res}\pi a^2 t u^2}{\frac{\rho_{gas}c_{gas}}{2} u^2 \pi a^2 \frac{1}{f}} = \frac{\rho_{res} t f}{\rho_{gas} c_{gas}}. \tag{3.7}$$

Thus the dissipation from sound radiation is predicted to scale as

$$Q^{-1} = \frac{\rho_{gas} c_{gas}}{\rho_{res} t f} \tag{3.8}$$

where t is the device layer thickness, c is the speed of sound in the gas, and ρ represents the density of the gas or the drum. We find that Equation 3.8 predicts a quality factor $Q = 19$ at $P_a = 1$ atmosphere compared to a $Q \approx 30$ observed for the fundamental mode, f_{01}. The discrepancy most likely arises due to the non-uniform motion of the drum across its diameter. We examine the dissipation and frequency shift of harmonics of the resonator extending from the fundamental mode to modes with frequencies greater than 140 MHz and find Equation 3.8 to be consistent with the observed linear increase in Q with mode frequency, shown for a drum in Figure 3.5.

Drum resonators show sufficient frequency shift to function as pressure sensors in the Torr regime with linear response and high sensitivity (over $2kHz/Torr$ in 95 nm gap devices) across this range. Moreover, the geometry of the devices has been

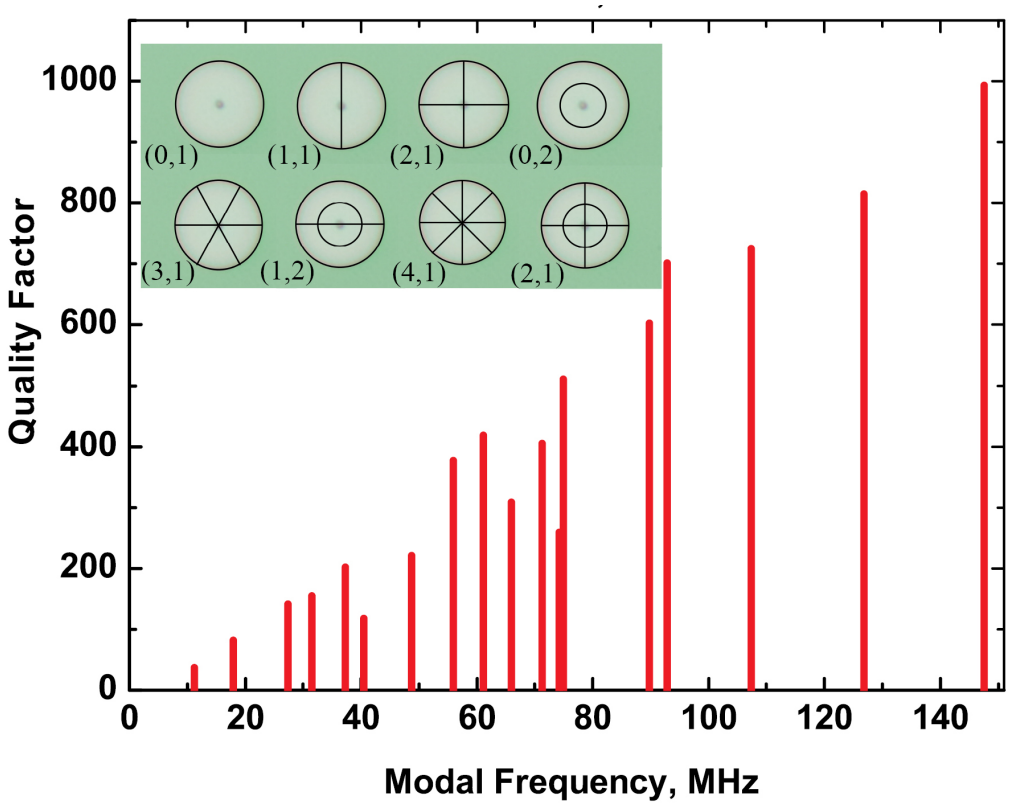

Figure 3.5: The Q of out-of-plane modes of a drum resonator at 1 atmosphere pressure varies linearly with frequency. Inset: Mode shapes of first several modes.

optimized for efficient electrical drive and detection [33], and this effect has been demonstrated by these means. Compatibility with electrical detection methods, such as capacitive detection or the embedding of a piezoresistive strip [21] facilitates future integration with conventional electronics. Squeeze film pressure transducers are self-equilibrating and gas species-independent. The uncomplicated fabrication of drum-type resonators likewise lends itself to realizable pressure transducers, and potentially to integration into CMOS foundry processes [22, 23].

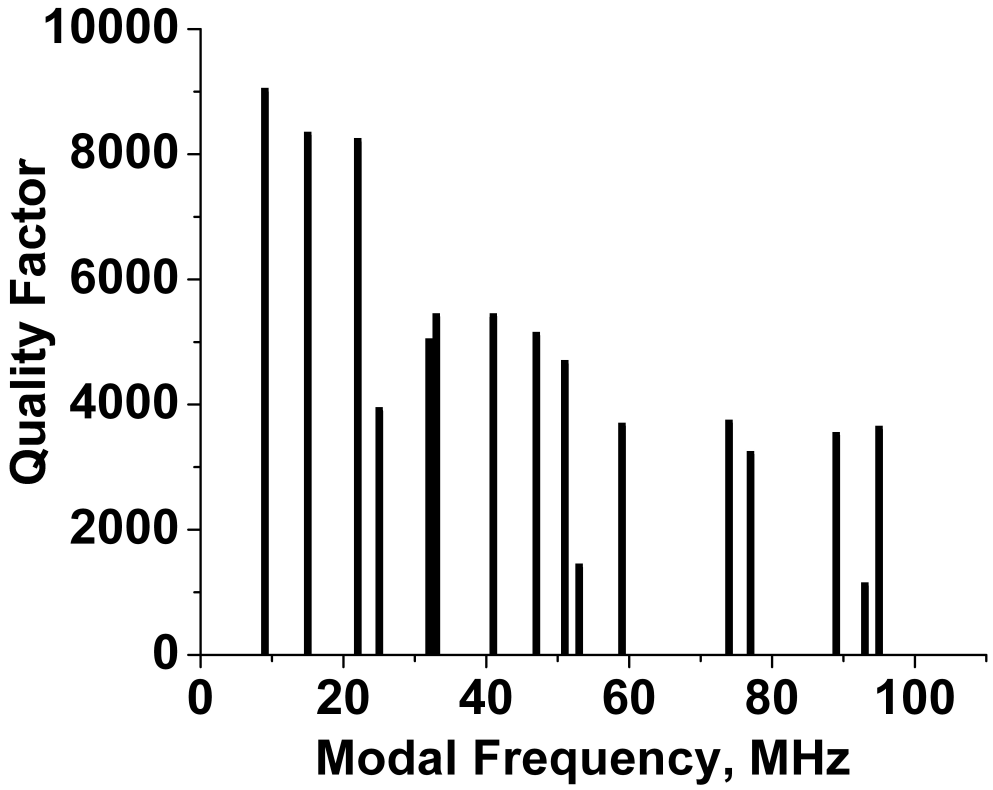

Figure 3.6: The Q of out-of-plane modes of a drum resonator at in vacuum varies linearly with frequency.

3.7 Conclusion

In summary we utilize the squeeze film effect to demonstrate a pressure-induced linear increase in the resonance frequency of a drum resonator. The gas in the squeeze film trapped under the membrane is clamped by viscous effects and does not flow out of the central etch orifice, effectively creating a self-equilibrating closed volume. The dissipation ($\frac{1}{Q}$) is found to be independent of orifice size and squeeze film thickness. We show that acoustic losses dominate energy dissipation and that operation at higher frequency results in smaller loss, extending the potential

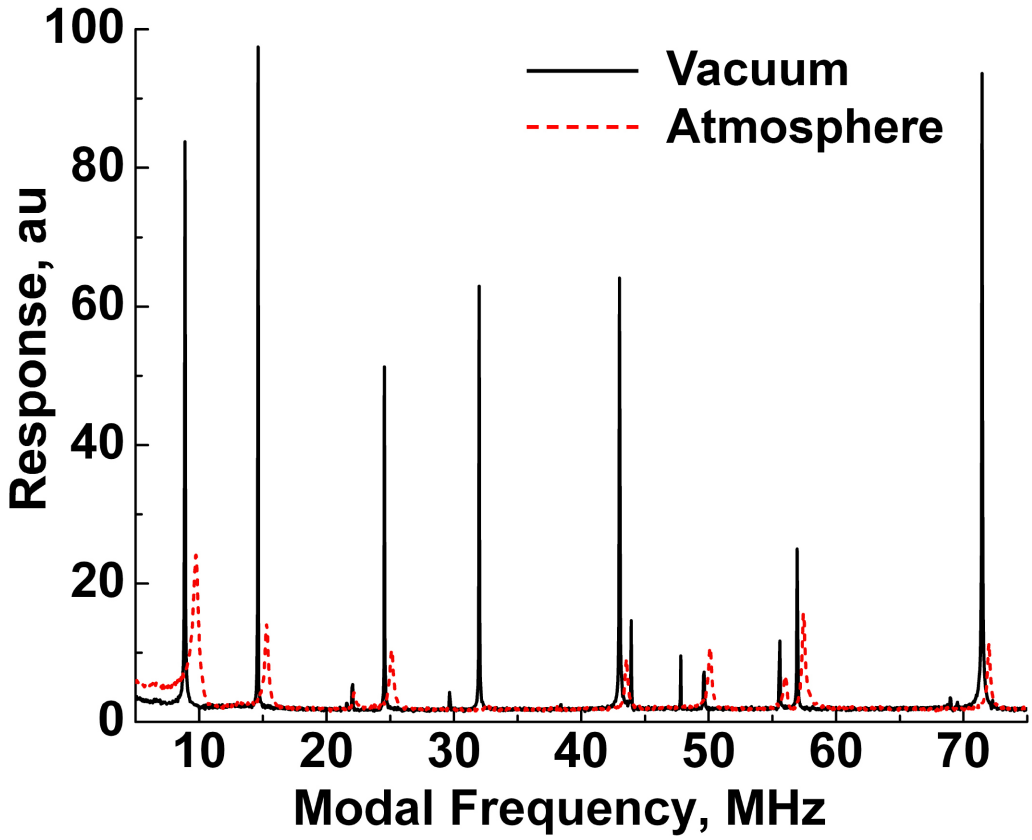

Figure 3.7: Positive frequency shift in the spectrum of a drum resonator with a 223 nm cavity as the pressure is changed from 35 mTorr (solid line) to 1 atm pressure (dashed line).

usability of these structures.[2]

[2]Research was supported by DARPA under Grant No. HR0011-06-1-0042, and NSF IGERT Grant No. DGE-0654193.

BIBLIOGRAPHY

[1] B. Ilic and H. G. Craighead and S. Krylov and W. Senaratne and C. Ober and P. Neuzil, Journal of Applied Physics **95** 7 3694-3703 (2004)

[2] Y. T. Yang and C. Callegari and X. L. Feng and K. L. Ekinci and M. L. Roukes, Nano Letters **6** 4 583-586 (2006)

[3] S. S. Verbridge and L. M. Bellan and J. M. Parpia and H. G. Craighead, Nanoletters **6** 9 2109-2114 (2006)

[4] M. Zalalutdinov and K. L. Aubin and R. B. Reichenbach and A. T. Zehnder and B. Houston and J. M. Parpia and H. G. Craighead, Applied Physics Letters **83** 18 3815-3817 (2003)

[5] D. W. Carr and H. G. Craighead, Journal of Vacuum Science & Technology B **15** 6 2760-2763 (1997)

[6] W. S. Griffin and H. H. Richards and S. Yamanami, Journal of Basic Engineering **88** 2 451 (1966)

[7] W. E. Newell, Science **161** 1320 (1968)

[8] J. J. Blech, Journal of Lubrication Technology **105** 4 615-620 (1983)

[9] F. Pan and J. Kubby and E. Peeters and A. T. Tran and S. Mukherjee, Journal of Micromechanics and Microengineering **8** 3 200-208 (1998)

[10] H. V. Allen and S. C. Terry and D. W. Debruin, Sensors and Actuators **20** 1 153-161 (1989)

[11] M. H. Bao and H. Yang, Sensors and Actuators A-Physical **136** 1 3-27 (2007)

[12] T. Veijola, Microfluidics and Nanofluidics **6** 2 203-219 (2009)

[13] S. S. Verbridge and R. Ilic and H. G. Craighead and J. M. Parpia, Applied Physics Letters **93** 1 15002 (2008)

[14] M. Andrews and I. Harris and G. Turner, Sensors and Actuators A–Physical **36** 1 79-87 (1993)

[15] M. K. Andrews and G. C. Turner and P. D. Harris and I. M. Harris, Sensors and Actuators A–Physical **36** 3 219-226 (1993)

[16] Thesis of Keith Aubin, Cornell University, 2005

[17] T. Veijola and A. Pursula and P. Raback, Journal of Micromechanics and Microengineering **15** 9 1624-1636 (2005)

[18] R. B. Bhiladvala and Z. J. Wang, Physical Review E **69** 3 36307 (2004)

[19] L. D. Landau and E. M. Lifshitz, *Fluid Mechanics*, 2^{nd} ed. (Oxfordshire, Oxford, 1987), p.285

[20] Patrick A. Truitt and Jared B. Hertzberg and C. C. Huang and Kamil L. Ekinci and Keith C. Schwab, Nano Letters **7** 1 120-126 (2007)

[21] R. B. Reichenbach and M. Zalalutdinov and J. M. Parpia and H. G. Craighead, IEEE Electron Device Letters **27** 10 805-807 (2006)

[22] J. L. Lopez and J. Verd and J. Teva and G. Murillo and J. Giner and F. Torres and A. Uranga and G. Abadal and N. Barniol, Journal of Micromechanics and Microengineering **19** 1 15002 (2009)

[23] G. K. Fedder and R. T. Howe and T. J. K. Liu and E. P. Quevy, Proceedings of the IEEE **96** 2 306-322 (2008)

CHAPTER 4

STRESS-BASED VAPOR SENSING USING FUNCTIONALIZED MICROMECHANICS

4.1 Abstract

We demonstrate that silicon-polymer composite microbridges provide a robust means of water vapor detection at ambient pressure. Volumetric changes in the reactive polymer alter the tension in a doubly-clamped structure leading to large and rapid changes in the resonance frequency. We demonstrate stress-based sensing of water vapor in ambient pressure nitrogen using doubly-clamped buckled beams coated with a hygroscopic polymer. We show stress sensitivity of around 20 kPa ($\sim$170 ppb of water vapor) and sub-second response time for coated microbridges.[1]

4.2 Introduction

A need exists for fast and inexpensive trace-vapor detectors. Microsensors based on electrochemical, surface acoustic wave, optical and mechanical transduction are under investigation to meet this demand [1]. Sensors based on microelectromechanical systems (MEMS) are candidates for a wide range of sensing applications including environmental monitoring [2]; bio- and health analysis [3, 4, 5, 6]; and detection of explosives for security use and landmine sweeping [7, 8, 9, 10].

Microcantilevers have been the primary MEMS structures used in sensors research. In these studies, changes in the resonance frequency of the cantilever due to the added mass of analyte or changes in materials properties due to chemical in-

[1]This chapter is based on a manuscript published in Applied Physics Letters and reprinted with permission from Darren R. Southworth, Leon M. Bellan, Yoav Linzon, Harold G. Craighead, and Jeevak M. Parpia, "Stress-based vapor sensing using resonant microbridges", *Applied Physics Letters* **96** 16 163503, April 2010. Copyright 2010, American Institute of Physics

teraction between the analyte and a reactive coating are measured. Intertial mass sensors have proven extremely sensitive in vacuum [11, 12, 13]. Various surface coatings and treatments have been developed for use at ambient pressure where sensitivity is lower in resonant devices due to viscous losses [9, 14, 15, 16]. Alternately, cantilevers are coated on a single side with a reactive layer that swells or contracts upon contact with an analyte and a static deflection is measured [17]. In functionalized cantilever studies, deflection of the composite structure relieves the stress induced by these volumetric changes.

In contrast to these mechanisms, in this chapter we demonstrate that the stress from the swelling of a reactive coating can be quantifiably measured by tracking shifts in the resonance frequency of a microbridge. Microbridges ($25\times6\times0.12$ μm) are fabricated from compressively-stressed polycrystalline silicon films grown by low pressure chemical vapor deposition (LPCVD) over a sacrificial oxide layer. See further fabrication details in A.1. Upon wet-etch release of a doubly-clamped bridge, the residual stress is relieved by buckling of the structure (toward the substrate in the case of this experiment), as depicted in Figure 4.1.

We deposit 100 nm of a porous hygroscopic polymer, tert-butylcalix[6]arene (TBC6A), by thermal evaporation onto the bridge. This material has been considered for detection of trinitrotoluene (TNT) vapors [9] but is shown here to be strongly affected by moisture. Porous polymers commonly swell in proportion to the relative humidity [20], and the frequency of tensile-stressed doubly-clamped all-polymer beams has been shown to decrease with hygrometric expansion and the associated reduction of the included tension [21].

The resonant behavior of these buckled beams has been described by Nayfeh and Emam *et. al.* [18, 19]. Swelling of the polymer layer in a composite buckled beam configuration (where the buckling occures as a response to compressive

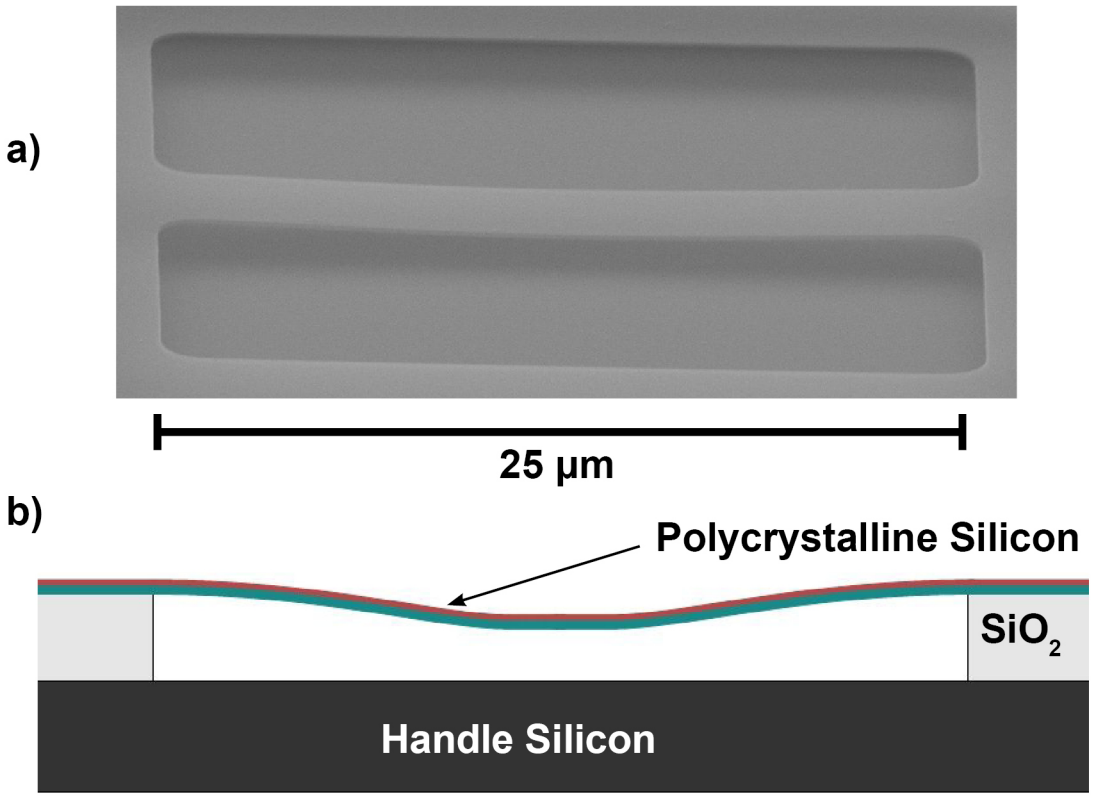

Figure 4.1: a) SEM of compressively-stressed polycrystalline silicon "buckled beam" bridge resonator. b) Cartoon of buckled beam depicted with sensitive coating (TBC6A, red layer).

stress), however, produces an axial load that increases the resonance frequency of the fundamental mode. The frequency response of a coated microbridge to water vapor is shown in Figure 4.2. These shifts are counter to the effect of added mass, Δm, which reduces the natural frequency as $\Delta f = -\frac{1}{2} f \frac{\Delta m}{m_{\text{eff}}}$, where f is the frequency and m_{eff} is the effective mass of the resonator. Although we do not know the difference in density between a dry and saturated polymer coating, if we presume, for example, that 15% of the volume of this porous polymer is filled

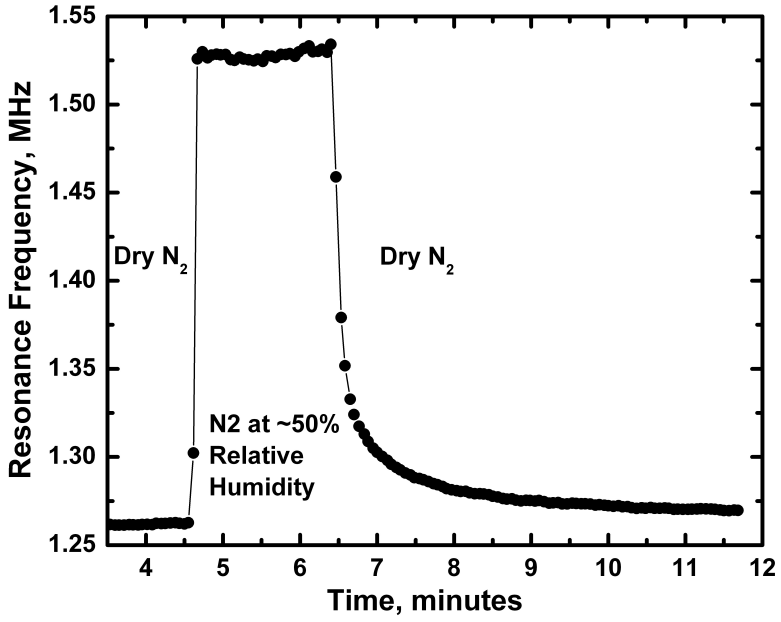

Figure 4.2: Fast rise in natural frequency of a buckled polycrystalline silicon microbridge resonator coated in a hygroscopic polymer in response to an increase in relative humidity in nitrogen from dry to around 50%. The frequency increases with volumetric expansion of the polymer coating due to the buckled nature of the bridge. Data points are acquired at three-second intervals and the desaturation curve originates from systematic drying of the vapor lines of the experimental setup, shown in Figure 4.4.

with liquid water—an intensional exageration—we find that the percent difference in mass, $\frac{m_{wet}-m_{dry}}{m_{dry}} \approx 4\%$, thus a drop in natural frequency of $\sim$2%, or 25 kHz in the case of a 1.25 MHz beam. We estimate that such mass loading decreases the resonance frequency by less than 25 kHz, small compared to the frequency increase observed, and we neglect the added water mass in further calculations assuming the stress-induced frequency rise overwhelms any inertial mass-based frequency reduction. The relationship between the change in thickness from stiffness and the structural stiffness, with the presumed change in Young's modulus, has not been

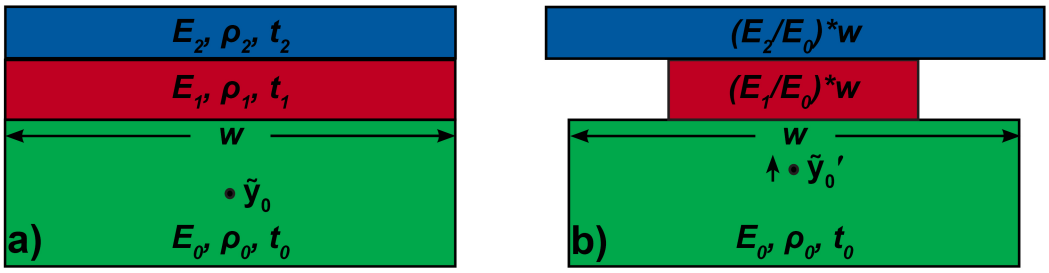

Figure 4.3: a) Original and b) modified multi-layer beam cross-section, width w, thickness t, original centroid $\widetilde{y_0}$ and modified centroid $\widetilde{y_0}'$. Here, $E_1 > E_0 > E_1$.

considered.

Applying the equivalent beam method of Timoshenko [22] to our composite beams we find that the flexural rigidity (EI, where E is the Young's modulus; I is the moment of inertia, $I = \frac{1}{12}wt^3$; w is the width and t is the thickness) is changed by roughly 4% by the addition of the polymer. This is calculated as follows, and with further elaboration available from [22] or from the excellent thesis of Philip Waggoner, 2009 [23].

In the equivalent beam method, a beam constructed of multiple layers is modeled to be homogeneous with respect to the Young's modulus. The width of each layer is scaled by its actual Young's modulus, and the moment of inertia around the new centroid is found, as in Figure 4.2. The densities and thicknesses are considered constant, and the new centroid of an n-layer beam is found by

$$\bar{y}' = \frac{\Sigma(\widetilde{y}_n A_n)}{\Sigma A_n}, \tag{4.1}$$

where A_n is the cross-sectional area of a layer and $\bar{y}_n$ is the centroid. The new second moment of inertia is found around $\bar{y}'$ by using the parallel axis theorem,

$$I' = \Sigma(I_n + A_n(\widetilde{y}_n - \widetilde{y})^2). \tag{4.2}$$

Using the nominal values for Young's modulus $E_{Si} = 10^{11}$ and $E_{polymer} = 10^9$ and equal layer thicknesses to find the new equivalent width of the polymer layer, $w_{polymer} = \frac{E_{polymer}}{E_{Si}} w_{Si} = 0.01 w_{Si}$. From this and Equation 4.1 we find

$$\widetilde{y}' = \frac{t_0}{2}\left(\frac{1 + 3\frac{E_1}{E_0}}{1 + \frac{E_1}{E_0}}\right) = \frac{t_0}{2}\left(\frac{1.03}{1.01}\right). \tag{4.3}$$

Equation 4.2 then expands to

$$I' = \frac{1}{12} w_0 t_0^3 + w_0 t_0 \left(\frac{t_0}{2} - \widetilde{y}'\right) + \frac{1}{12} w_1 t_1^3 + w_1 t_0 \left(\frac{3}{2}\frac{t_0}{2} - \widetilde{y}'\right). \tag{4.4}$$

Assuming $\widetilde{y}' \approx t_0$, Equation 4.4 reduces to

$$I' = \frac{1}{12} w_0 t_0^3 \left[1 + 4\frac{E_1}{E_0}\right] \approx I_0 \times 1.04 \tag{4.5}$$

in the case of equal layer thicknesses. However $t_{Si} = 130$ nm and $t_{polymer} < 100$ nm in most devices tested. Thus in this configuration the main role of the polymer is to alter stress, since the polymer does not significantly affect the flexural rigidity of the composite structure.

The experimental setup is depicted in Figure 4.4. In this experiment, MEMS are electrostatically driven and their motion is detected optically using an interferometric technique [24] through the window of a flow cell. The resonance spectrum of the microbridges is monitored in real-time as the relative humidity of the nitrogen is varied between zero and nearly 100%. The relative humidity is controlled using a pair of mass flow controllers that vary the mixing ratios of dry nitrogen and nitrogen aerated through a column of deionized water. Although no humidity standard was used in this experiment, we assume the aerated nitrogen to be fully saturated.

Devices are placed in a flow cell of volume 0.7 cm^3 (6.5 mm diameter bore, 1 cm depth) under continuous flow conditions of 20 sccm. The volume of the flow lines are not relevant here since they are presumed to flush without mixing. We observe

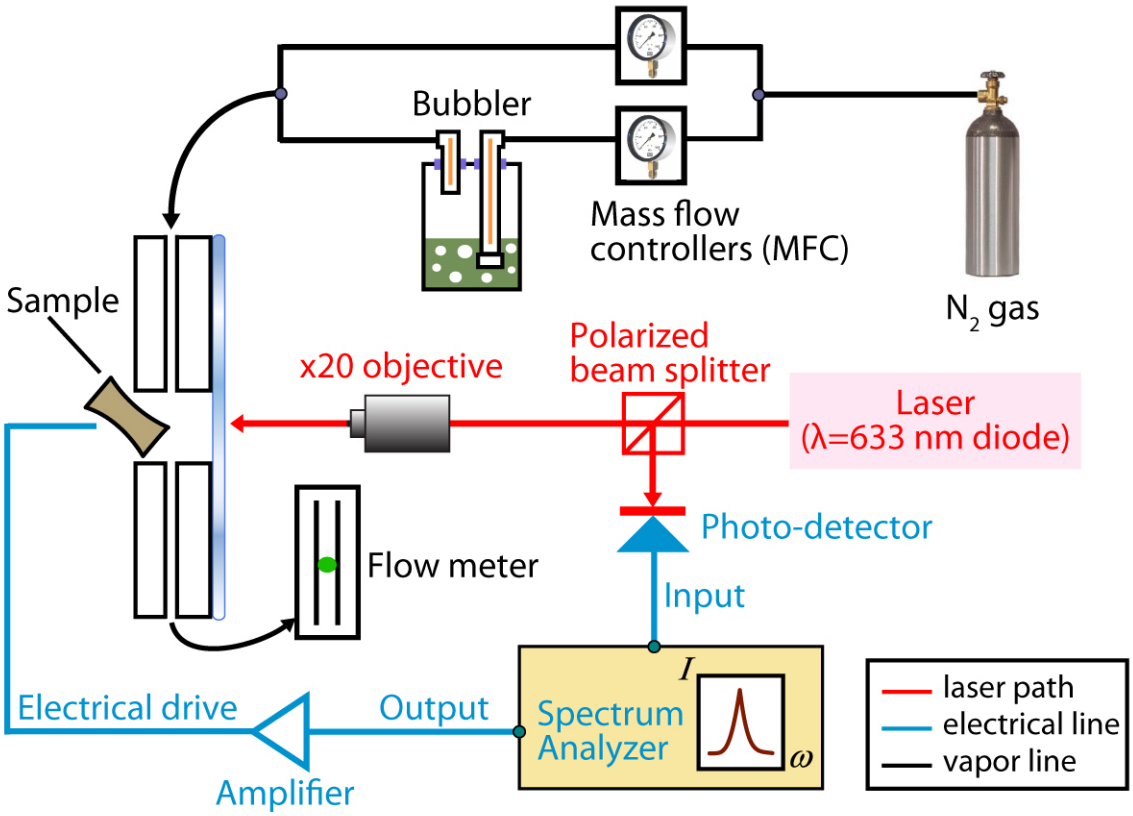

Figure 4.4: Schematic of the experimental setup including electrical drive, optical detection, and vapor delivery system.

that the characteristic time for the device to stabilize at a new frequency, or its rise time, changes in accordance with the flow cell time constant, $\tau = \frac{cell\ volume}{flow\ rate}$, for varied gas flow rates, which do not otherwise affect device performance. For example, $\tau = \frac{0.7cm^3}{20cm^3/min} = \frac{0.7cm^3}{0.66cm^3/s} \approx 1s$. From this we determine that the rise time is set in this experiment by the time required to replace the gas in the flow cell volume. Thus the characteristic resonator response time is shown to be below one second. The longer time constant for the desaturation curve in Figure 4.2 is believed to result from the time associated with the systematic drying of the flow lines, although we cannot rule out slower water desorption kinetics.

4.3 Theory

Development of beam theory has a mathematical history dating to Euler, or even Galileo's enquiry or the enunciation of Hooke's Law, but only recently have theorists developed an exact analytical solution to the resonant behavior of buckled beams [19]. If the nonlinear, damping and forcing terms are dropped from the differential equation of motion, the resonant frequency relationship to the axial (compressive) load of a buckled beam may be obtained in closed form.

The buckled beam theory is adapted from the 2008 Nonlinear Dynamics article by Ali Nayfeh of Virginia Tech and Samir Emam Zagazig University in Egypt, *Exact solution and stability of postbuckling configurations of beams* [19]. In their derivation they find

$$\omega^2 = 2\lambda^4(\frac{S}{\lambda^2} - 1), \tag{4.6}$$

where ω is the non-dimensional angular frequency, which in this unforced, undamped resonator is given by

$$\omega = \hat{\omega}\sqrt{\frac{m_l l^4}{EI}} \tag{4.7}$$

where $\hat{\omega}$ is the dimensional angular frequency. Here, m_l is the per-length mass, l is the undeformed length of the beam, and S is the non-dimensional axial load on the doubly-clamped beam. The non-dimensional applied axial force, S is given by

$$S = \frac{\hat{S}l^2}{EI} \tag{4.8}$$

and yields the dimensional axial force $\hat{S}$. The critical buckling load, λ^2, in non-dimensional units comes out to 2π.

Plugging in Equations 4.7 and 4.8 into Equation 4.6 dimensionalizes it and yields

$$\omega^2 = \frac{8\pi^2}{m_l l^2}(\hat{S} - 4\pi^2\frac{EI}{l^2}). \tag{4.9}$$

Equating $\omega = 2\pi f_0$ and solving for f_0 yields Equation 4.10,

$$f_0 = \sqrt{\frac{2}{m_l l^2}(\hat{S} - 4\pi^2 \frac{EI}{l^2})}. \tag{4.10}$$

This simple form may simplify many practical applications. In the following section we apply Nayfeh's theory to our buckled beams.

4.4 Results

Ignoring the added water mass and changes in the Young's modulus of the polymer, the stress in the buckled beam may be calculated directly from the resonant frequency measurements, as shown in Figure 4.5. The second term under the radical in Equation **??** describes the critical load at which the beam buckles and the resonance frequency drops to zero. In our devices this load corresponds to an axial (compressive) stress of 5.5 MPa, depicted in the fit of the data in Figure 4.5. The inbuilt stress, 7.6 MPa (that exceeds the buckling stress), results in the static bowing of the beam. Swelling of the polymer when exposed to nitrogen over the full humidity range produces an additional axial stress of around 2.2 MPa. The linearity of the hygrometric expansion of the polymer is generalized to TBC6A from Buchhold [20] and yields the hygrometric strain $\epsilon_{\text{hyg}} = \alpha_{\text{hyg}} RH$, where α_{hyg} is the linear coefficient of hygrometric expansion and RH stands for the relative humidity, which varies between zero and one. The stress imparted by polymer swelling is thus

$$\sigma_{\text{hyg}} = \Delta\sigma = E_{\text{Si}} \alpha_{\text{hyg}} RH. \tag{4.11}$$

From Equation 4.11 and the measured change in frequency of a microbridge with RH we calculate the coefficient of humidity-induced volume expansion to be $\alpha_{\text{hyg}} = 18$ ppm. We find that the frequency stability of the resonators limits our resolution to 3 kHz in the limit of low humidity, see baseline of Figure 4.2. In

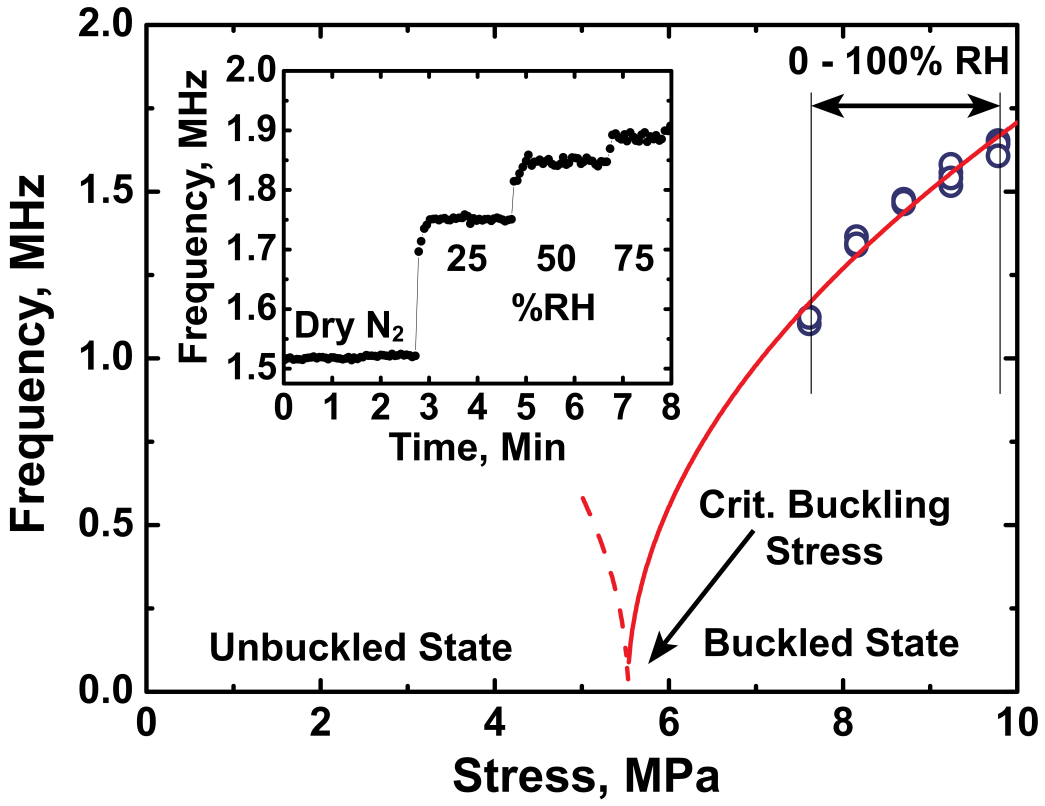

Figure 4.5: Changes in resonance frequency of a buckled beam. A hygrometric polymer coating expands in proportion to relative humidity *(RH)*. Extrapolation of the fit to the data illustrates potential for high sensitivity near the critical buckling stress. Inset: Resonance frequency shift of a coated microbridge in response to stepped changes in relative humidity. Variation in frequency among the devices presented arises from varied timing in the release step.

our experiment, 3 kHz resolution corresponds to a minimum detectable change in stress of ∼20 kPa, or 170 ppb of water vapor.

4.5 Discussion

Sensors operated near the critical stress of buckling could show greatly increased stress sensitivity since the frequency-stress curve becomes steep as the stress ap-

proaches the critical stress. The maximum stress sensitivity obtainable is likely to be set by geometrical imperfections in the beam [26, 27], which in effect smooth the transition from the unbuckled to the buckled state. The stress sensitivity of a microbridge varies strongly with the silicon layer thickness, and thus in detector applications these structures benefit from the thin films available in MEMS processing. When optimized, thin microbridges operating near the critical buckling stress could provide a very high sensitivity platform for sensing.

Improved resolution of frequency for operation in gas is possible through improvement of the quality factor, Q, by optimization of the device geometry. Measurements of bare and coated microbridges in vacuum yield nominal Q of 4000 and 400 respectively, compared to a quality factor of at most 10 in air ($Q = 3$ for 6 μm wide beams; $Q = 10$ for 2 μm wide beams). This suggests that acoustic dissipation (viscous damping) rather than intrinsic materials loss is the primary energy dissipation mechanism at atmospheric pressure [28]. The vacuum quality factor of 400 for the composite structure implicates intrinsic losses in the polymer as the predominant dissipation mechanism in vacuum [29]. Air damping in resonant MEMS remains an active area of research [30, 31]. Studies of resonant operation of MEMS at atmospheric pressure suggest a path toward decreased dissipation, $(1/Q)$, by taking advantage of higher frequencies to decrease acoustic coupling to air [28, 13].

Microbridges enable direct transduction of stress variation into the frequency or phase domain, which is advantageous for its high measurement accuracy and for integration of sensors into radio frequency circuitry. Structures created from doped silicon, such as ours, are compatible with the electrical detection techniques introduced by Truitt *et. al.* [33] and discussed in Chapter 2, as well as amenable to readout via embedded piezoelectric elements [12]. Because of their different

responses to stress, operation of microbridges in conjunction with cantilevers or other variously coated, sensitive structures could contribute an orthogonal response to assist in unique identification of analytes in electronic nose applications.

4.6 Conclusion

We have shown that resonant microbridges coated with TBC6A can be sensitive to relative humidity. While this material has been shown to be sensitive to other volatile compounds, those wishing to employ hygroscopic materials for detection must control carefully for moisture. Common mode canceling can be employed to account for environmental factors such as atmospheric pressure or temperature variations.

Stress-based resonant sensing using microbridges represents an unexploited method for detection of vapors applicable to electronic noses operating in ambient conditions. Surface coatings under development for deflection-based cantilever sensors can be applied to doubly-clamped structures where the fast response and readout in the frequency domain commend them to sensor applications. Doped polycrystalline silicon resonators such as those described in this work are compatible with electrical detection and integration into industrial CMOS processes [35, 36], where stressed polycrystalline silicon layers are common. Fabricated through simple top-down processing, microbridge sensors represent an excellent example of advantageous scaling in MEMS. Resonant detection of vapor through the mechanism of stress has potential to improve real-time atmospheric gas sensing technology.[2]

[2]Fabrication was performed at the Cornell Nano-Scale Science and Technology Facility. This research was supported by Analog Devices and DARPA under HR-00011-06-0042 and by the NSF under DMR-0908634. We thank Joshua Cross, Philip Waggoner, and Elaine Guidero for their assistance and commentary.

BIBLIOGRAPHY

[1] S. Singh, Journal of Hazardous Materials **144** 1 15-28 (2007)

[2] M. R. Plata and J. Hernando and M. Zougagh and A. M. Contento and M. J. Villasenor and J. L. Sanchez-Rojas and A. Rios, Sensors and Actuators B–Chemical **134** 1 245-251 (2008)

[3] T. Braun and M. K. Ghatkesar and N. Backmann and W. Grange and P. Boulanger and L. Letellier and H. P. Lang and A. Bietsch and C. Gerber and M. Hegner, Nature Nanotechnology **4** 3 179-185 (2009)

[4] H. F. Ji and H. Y. Gao and K. R. Buchapudi and X. Yang and X. H. Xu and M. K. Schulte, Analyst **133** 4 434-443 (2008)

[5] R. L. Gunter and W. D. Delinger and T. L. Porter and R. Stewart and J. Reed, Medical Engineering and Physics **27** 3 215-220 (2005)

[6] Yee Lam and Nehal I. Abu-Lail and Munir S. Alam and Stefan Zauscher, Nanomedicine-Nanotechnology Biology and Medicine **2** 4 222-229 (2006)

[7] J. C. Kapoor and G. K. Kannan, Defence Science Journal **57** 6 797-810 (2007)

[8] A. R. Krause and C. Van Neste and L. Senesac and T. Thundat and E. Finot, Journal of Applied Physics **103** 9 (2008)

[9] P. G. Datskos and N. V. Lavrik and M. J. Sepaniak, Sensor Letters **1** 1 25-32 (2003)

[10] L. A. Pinnaduwage and A. Wig and D. L. Hedden and A. Gehl and D. Yi and T. Thundat and R. T. Lareau, Journal of Applied Physics **95** 10 5871-5875 (2004)

[11] B. Ilic and H. G. Craighead and S. Krylov and W. Senaratne and C. Ober and P. Neuzil, Journal of Applied Physics **95** 7 3694-3703 (2004)

[12] Y. T. Yang and C. Callegari and X. L. Feng and K. L. Ekinci and M. L. Roukes, Nano Letters **6** 4 583-586 (2006)

[13] P. Thiruvenkatanathan and J. Yan and J. Woodhouse and A. Aziz and A. A. Seshia, Applied Physics Letters 96 8 081913 (2010)

[14] M. A. Urbiztondo and I. Pellejero and M. Villarroya and J. Sese and M. P. Pina and I. Dufour and J. Santamaria, Sensors and Actuators B-Chemical **137** 2 608-616 (2009)

[15] L. A. Pinnaduwage and V. Boiadjiev and J. E. Hawk and T. Thundat, Applied Physics Letters **83** 7 1471-1473 (2003)

[16] C. Zuniga and M. Rinaldi and S. M. Khamis and A. T. Johnson and G. Piazza, Applied Physics Letters **94** 22 (2009)

[17] G. Y. Chen and T. Thundat and E. A. Wachter and R. J. Warmack, Journal of Applied Physics **77** 8 (1995)

[18] A. H. Nayfeh and W. Kreider and T. J. Anderson, AIAA Journal **33** 6 (1995)

[19] A. H. Nayfeh and S. A. Emam, Nonlinear Dynamics **54** 4 395-408 (2008)

[20] R. Buchhold and A. Nakladal and G. Gerlach and K. Sahre and K. J. Eichhorn, Thin Solid Films **312** 1 232-239 (1998)

[21] S. Schmid and S. Kuehne and C. Hierold, Journal of Micromechanics and Microengineering **19** 6 065018 (2009)

[22] S.Timoshenko, *Strength of Materials* 2^{nd} ed. (Lancaster, New York, 1940) pp. 216-218

[23] Thesis of Philip Waggoner, Cornell University, 2009

[24] D. W. Carr and H. G. Craighead, Journal of Vacuum Science & Technology B **15** 6 2760-2763 (1997)

[25] L. Euler, *De motu oscillatorio corporum flexibilium* (Paris Academy of Sciences, Berlin 1751), Vol. 13, pp. 124-166

[26] W. Fang and J. A. Wickert, Journal of Micromechanics and Microengineering **4** 3 116-122 (1994)

[27] S. M. Carr and M. N. Wybourne, Applied Physics Letters **82** 5 709-711 (2003)

[28] D. R. Southworth and H. G. Craighead and J. M. Parpia, Applied Physics Letters **94** 213506 (2009)

[29] S. Schmid and C. Hierold, Journal of Applied Physics **104** 9 (2008)

[30] M. H. Bao and H. Yang, Sensors and Actuators A–Physical **136** 1 23-27 (2007)

[31] V. Cimalla and F. Niebelschuetz and K. Tonisch and C. Foerster and K. Brueckner and I. Cimalla and T. Friedrich and J. Pezoldt and R. Stephan and M. Hein and O. Ambacher, Sensors and Actuators B-Chemical **126** 1 24-34 (2007)

[32] S. S. Verbridge and R. Ilic and H. G. Craighead and J. M. Parpia, Applied Physics Letters **93** 1 15002 (2008)

[33] Patrick A. Truitt and Jared B. Hertzberg and C. C. Huang and Kamil L. Ekinci and Keith C. Schwab, Nano Letters **7** 1 120-126 (2007)

[34] Mo Li and H. X. Tang and M. L. Roukes, Nature Nanotechnology **2** 2 114-120 (2007)

[35] J. D. Cross and B. R. Ilic and M. K. Zalalutdinov and W. Zhou and J. W. Baldwin and B. H. Houston and H. G. Craighead and J. M. Parpia, Applied Physics Letters **95** 13 (2009)

[36] I. Voiculescu and M. E. Zaghloul and R. A. McGill and E. J. Houser and G. K. Fedder, IEEE Sensors Journal **5** 4 641-647 (2005)

[37] D. R. Southworth and L. M. Bellan and Y. Linzon and H. G. Craighead and J. M. Parpia, Applied Physics Letters **96** 163503 (2010)

CHAPTER 5

STRESS AND SILICON NITRIDE: A CRACK IN THE UNIVERSALITY OF GLASSES

5.1 Abstract

High-stress silicon nitride micro resonators exhibit a remarkable room temperature Q factor that even exceeds that of single crystal silicon. A study of the temperature dependent variation of the Q of a 255 μm $\times$ 255 μm $\times$ 30 nm thick high-stress Si_3N_4 membrane reveals that the dissipation, Q^{-1}, decreases with lower temperatures, and is $\simeq$3 orders of magnitude smaller than the universal behavior. Stress-relieved cantilevers fabricated from the same material show a Q that is more consistent with typical disordered materials. E-beam and X-ray studies of the nitride film's structure reveal characteristics consistent with a disordered state. Thus, it is shown that stress alters the Q^{-1}, violating the universality of dissipation in disordered materials in a self-supporting structure. [1]

[1]This chapter is based on a manuscript published in Physical Review Letters and reprinted with permission from Darren R. Southworth, R. A. Barton, B. Ilic, A. D. Fefferman, H. G. Craighead, and J. M. Parpia, "Stress and Silicon Nitride: A Crack in the Universal Dissipation of Glasses", *Physical Review Letters* **102** 225503, 5 June, 2009.

5.2 Introduction

Amorphous solids are by nature diverse in composition. Yet it is evident that there is a commonality to their low-energy vibrational spectrum as characterized by a universal dissipation, Q^{-1}, that "plateaus" as the temperature is varied between roughly 0.1 K and 10K at $1.5 \times 10^{-4} \leqq Q^{-1} \leqq 1.5 \times 10^{-3}$. The universality of glass was first noted by Zeller and Pohl [1]. The qualitative universality of glasses has been rather successfully explained in terms of the phenomenological tunneling model (TM) [3, 4], which assumes the presence of atomic tunneling entities with a broad distribution of energy splittings. The TM does not specify the identity of the tunneling entities, nor does it account for the quantitative universality of glassy properties noted in [2].

In this letter we describe temperature dependent measurements of dissipation Q^{-1} in high-stress self-supporting membranes and companion stress-relieved cantilevers resonated at their fundamental modes of excitation, and fabricated from silicon nitride, a disordered solid. While the former exhibit an internal friction that is three orders of magnitude below that of glassy systems (and within an order of magnitude of a bulk Si single crystal "paddle" resonator [5]), the stress-relieved cantilevers exhibit Q^{-1} close to values observed in glasses. The only other instances where an amorphous solid has demonstrated significant departure from the universal behavior were in hydrogenated amorphous silicon deposited by hot wire chemical vapor deposition [HWCVD] on single crystal silicon [5] (Q^{-1} was 200× smaller), and in other silicon nitride films also deposited on a silicon oscillator [6]. A larger silicon nitride membrane (f_0=135 kHz) exhibited comparable Q at 297 K [7], and high-stress metallized silicon nitride "nanostring" resonators with comparable Q to those measured in our laboratory at room temperature [8] were described by Schwab [9]. There are no reports of the temperature dependence of

bare self-supporting materials that reveal departures from the universal behavior till this work. No convincing quantitative explanation has been forthcoming in the intervening period of more than a decade since the initial publication [5].

There have been many attempts to question the underpinnings of the tunneling model itself. The issue of whether interactions between two-level systems play a role in the universality was raised by Yu and Leggett [10], and later by Burin and Kagan [11] and Kühn [12]. It was not till very recently that evidence for the contribution of interactions to Q^{-1} was reported in the literature [13], though there had been earlier reports of anomalous dissipation [14]. This evidence for interactions was only observed well below the universal plateau region. There has been other evidence for interactions between the tunneling entities in the dielectric behavior [15, 16]. These results were understood in terms of a hole in the distribution of TLS at zero local field (the "dipole gap") [17, 18]. In [19], the dipole gap theory was reconciled with acoustic measurements by noting that the effective range of TLS interactions increases as temperature decreases. Interactions are also cited as contributing to anomalous magnetic field dependent tunneling in glasses [20, 21, 22].

5.3 Devices and Measurement

The preparation of the Si_3N_4 film is germane to the properties realized. Standard (stoichiometric) silicon nitride is deposited by low pressure chemical vapor deposition (LPCVD) at 775°C in a 200 mTorr N_2 atmosphere. Once the temperature and pressure are stabilized, a 2-minute flow at 196 sccm (standard cm^3/minute) of ammonia is initiated, and a dichlorosilane flow at 60 sccm is maintained for the duration of the deposition. On completion of the deposition the dichlorosilane flow is turned off while ammonia flows for 2 minutes to react with any residual dichlorosi-

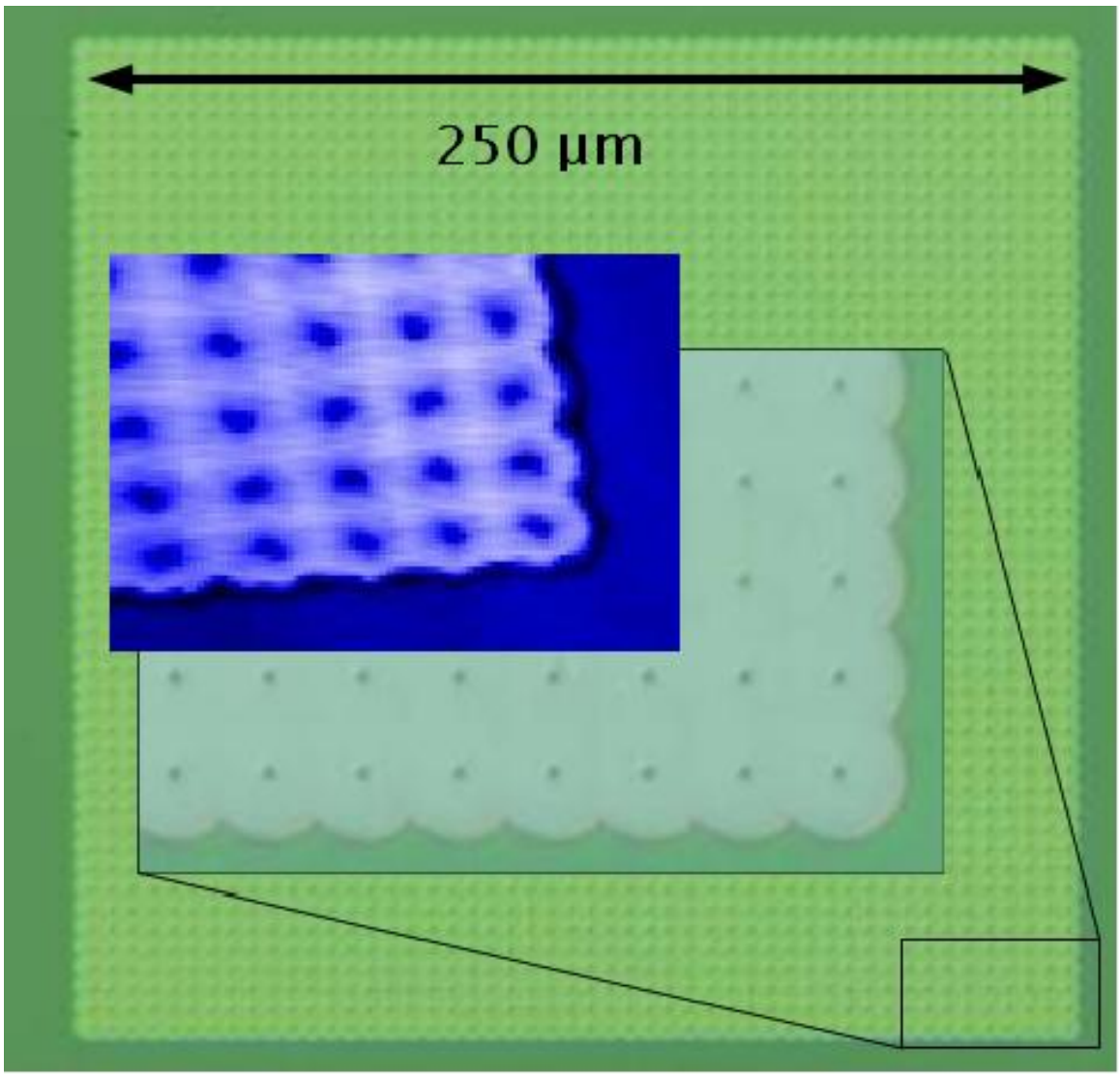

Figure 5.1: Image of a 255 μm $\times$ 255 μm $\times$ 30 nm thick silicon nitride resonator (the lighter region). Inset: A corner with 40 of the 50 $\times$ 50 0.8 μm diameter holes required to etch away the underlying SiO_2. Superimposed is an equivalent corner as imaged by the Attocube scanning stage.

lane. The process results in a high-quality silicon nitride film incorporating an included tensile stress (measured with a wafer-bow technique) of 1.20 ± 0.05 GPa that is about 0.63% of the bulk modulus [26]. The conditions are critical since low-stress nitride deposition takes place at 800°C and 200 mTorr, while dichlorosilane and ammonia flows are 126 sccm and 22 sccm respectively. The higher dichlorosilane flow creates a silicon-rich nitride that alleviates film stress. In contrast other processes [27] produce high-stress nitride that dissolves in the HF wet etch used to release the resonator.

In our laboratory we have shown that room temperature mechanical measurements on high-stress nitride exhibit a range of Q values depending on the geometrical configuration and size of the structure [8, 23]. We also demonstrated that in a given device, the mechanical distortion (bending) of the handle wafer supporting a film of low stress silicon nitride led to the enhancement of the film's Q [24]. It is well known that metallization increases Q^{-1}, therefore we developed a large scale non-metallized structure to facilitate the optical detection of resonant motion at low temperatures. The 110 nm-thick Si_3N_4 film was patterned with a 50×50 array of 0.8 μm holes spaced 5 μm apart. The holes admit HF to etch away the underlying 630 nm sacrificial oxide layer, yielding a 255 μm $\times$ 255 μm free-standing resonator attached to the wafer only around the periphery. The resonator's average thickness was reduced to $\sim$ 30 nm by the etch (estimate based on an observed 14 nm/min Si_3N_4 HF etch rate). The resonator is driven at its fundamental "drum-head" resonant frequency [25] around 1.5 MHz using a piezo disc that vibrates the chip in the out-of-plane direction. A high stress membrane is shown in Figure 5.1. To elucidate the role of stress on the dissipation, we also fabricated a silicon nitride cantilever resonator, which, because it is unsupported on three sides, has minimal included stress. A stress-relieved cantilever is shown

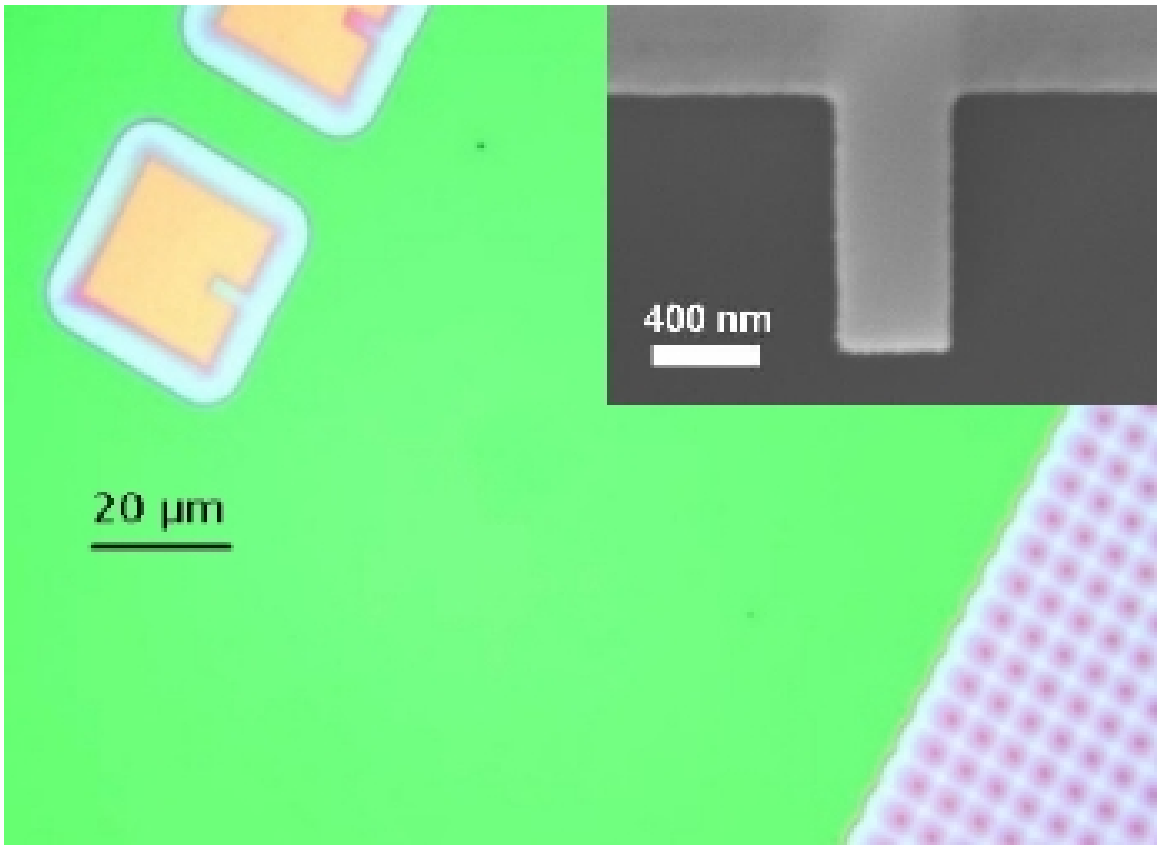

Figure 5.2: A stress-relieved cantilever near a 255 μm square resonator. An identical structure at the top is stuck to the underlying silicon and appears discolored. Inset: a SEM of a similar cantilever (smaller cantilever from array partially shown).

in Figure 5.2.

The devices' motion was detected optically [28] on a modified Attocube cryostat [29] operated in vacuum. 785 nm laser light was coupled to a low temperature objective lens via a single mode fiber and was reflected from the resonator-substrate assembly, the light collected and coupled to a photodiode connected to the input of a swept frequency network analyzer. The device and substrate comprise a Fabry-Perot interferometer. Motion of the resonator modulates the intensity of the reflected light. The resonant frequency, f_o of the structures (dictated by a combination of geometry, elastic properties of the material and temperature dependent

stress) was used as an internal thermometer to ensure that heating by the laser (or drive) was not significant. Because the differential expansion between the silicon handle wafer and the nitride dominates changes in the resonant frequency, we do not plot the temperature dependence here.

A single chip had identical resonators fabricated adjacent to one another. In a 3 × 3 array, all resonators exhibit $Q^{-1} \simeq 10^{-6}$ at room temperature with the exception of one structure with a Q ($\approx 10^4$) possibly due to a crack. The Q and f_o were obtained by fitting the response of the resonator to a lorentzian, and the Q was determined from the half-power width, Δf ($Q = f_o/\Delta f$). The resonators were driven at a small enough amplitude (estimated to be ≈1nm) to maintain a linear response (lorentzian lineshape and negligible frequency shift with amplitude). The response of membrane and cantilever resonators are shown in Figure 5.3.

5.4 Discussion

The temperature dependence of the internal friction, along with typical values observed for crystalline silicon and amorphous SiO_2 [6] are plotted in Figure SiNdissipation. At room temperature the internal friction of the Si_3N_4 resonator is lower than that measured for silicon double-paddle resonators (solid red line in Fig. 3), but the ∼ two-orders-of-magnitude decrease in Q^{-1} of the Si as the temperature is lowered is not observed in the glassy resonator. The contrast with the behavior expected for glasses is all the more striking with the high-stress nitride displaying a three-orders-of-magnitude lower dissipation than SiO_2.

The temperature dependent dissipation of the stress-relieved cantilevers is plotted in Figure 5.4 and is below the band of values seen in glasses (blue bar) by ∼ a factor of two. Thus, it is clear that the dissipation of the LPCVD stress-relieved film is more consistent with typical glassy behavior and is within an order of mag-

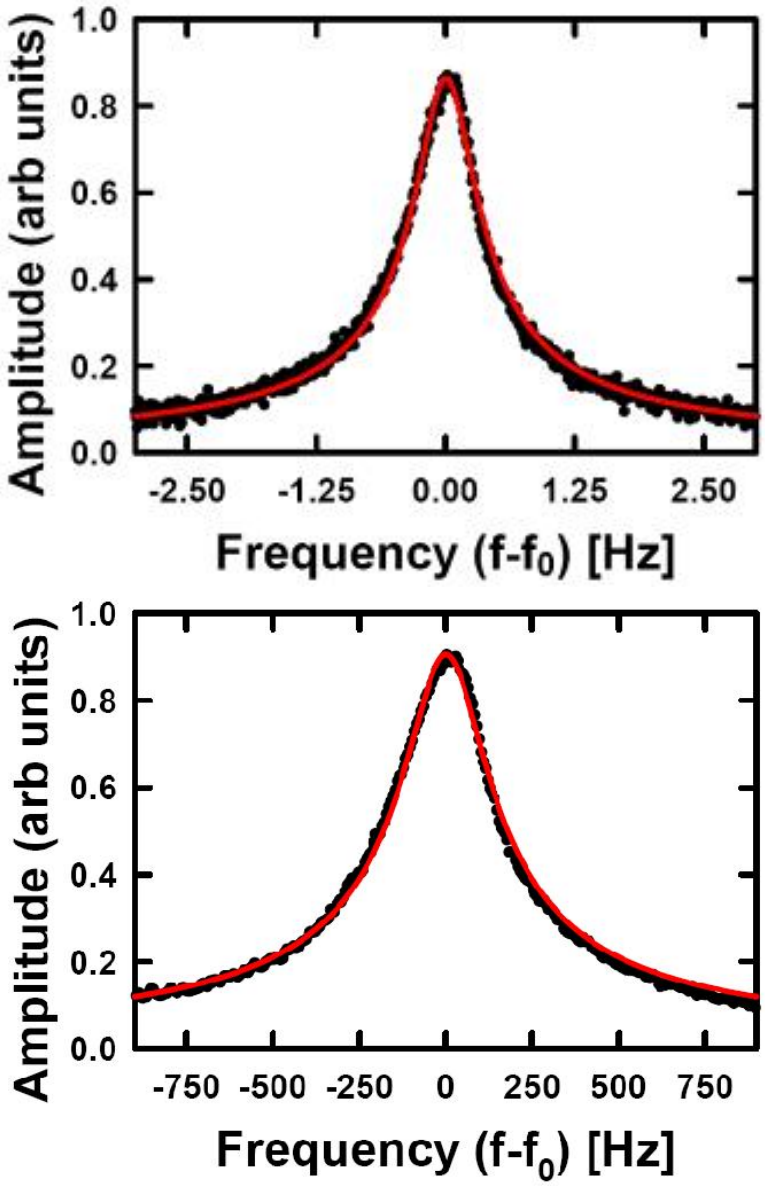

Figure 5.3: The amplitude response (points) and fits (solid lines) for a high-stress membrane (left, f_o=1.526445 MHz, Q=2.68×10^6) at 4.76 K, and stress-relieved cantilever resonator (right, f_o=3.538700 MHz, Q=1.48×10^4) at 4.7 K.

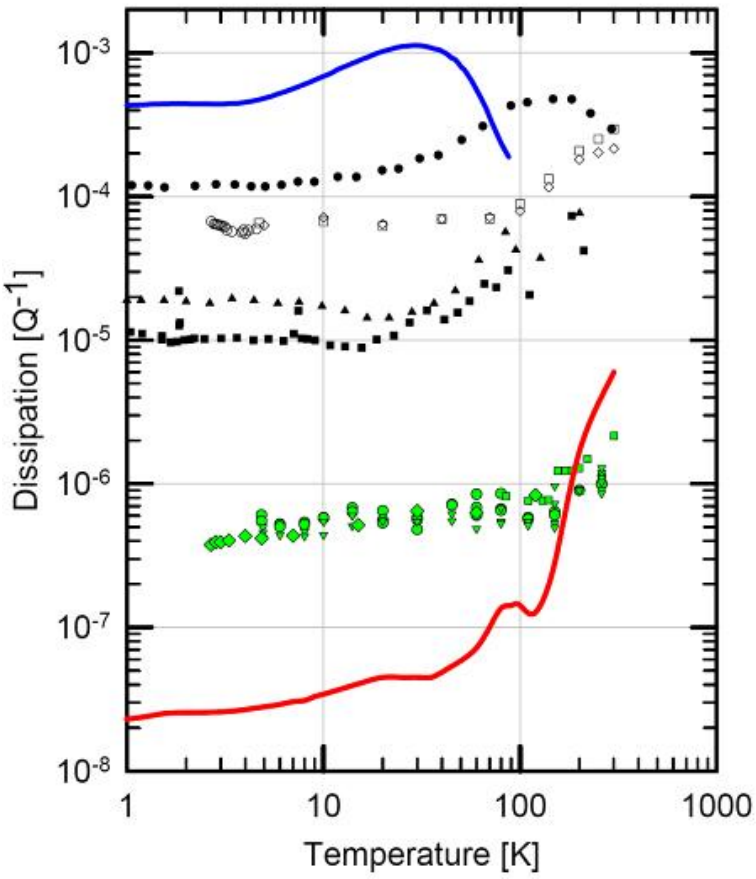

Figure 5.4: Temperature dependent internal friction measured for our high-stress LPCVD Si_3N_4 membrane structures. This is contrasted with the behavior of a-SiO_2 (solid blue line) and single crystal Si (solid red line)[5]. The range of "plateau" region values of Q^{-1} for a-SiO_2 is shown by the blue bar. We also show for comparison, results for e-beam deposited a-Si[5], and supported LPCVD films of SiN[6]. Our data on cantilever structures fabricated from the same LPCVD film as the high Q membranes show Q^{-1} a factor of $\sim$2 below the lower extent of the band consistent with other glassy materials.

nitude of results reported by Liu *et al.*[6].

In order to verify that the silicon nitride material is disordered, we examined an unreleased high-stress sample grown in the same batch. X-ray diffraction scans taken using a Scintag ID3000 spectrometer and general area detector diffraction system (GADDS) show a broad flat scattering region below 20 degrees, the result of diffraction from an amorphous material in contrast to peaks which would be characteristic of crystalline order, Figure 5.5. We also obtained TEM images of our $Si_3N_4/SiO_2/Si$ composite structure. These reveal no long range order: while the lattice in the Si (wafer) is clearly revealed, no such structure is seen from the images captured from the SiO_2 or Si_3N_4, Figure 5.6. This conclusion is supported by conventional e-beam diffraction and convergent beam electron diffraction (CBED). We conclude that the high-stress Si_3N_4 is not crystalline.

According to the tunneling model, the internal friction Q^{-1} of glasses in the plateau region is given by [5]

$$Q^{-1} = \frac{\pi}{2}\frac{\overline{P}\gamma^2}{\rho\nu^2}. \tag{5.1}$$

where $\overline{P}$ is the spectral density of tunneling states, γ is the coupling energy of the tunneling states to the lattice, ρ is the mass density, and ν the sound velocity. This expression (and the TM) are strictly applicable below 1K where thermally activated reorientations of the tunneling entities are negligible. Nevertheless, it is a general experimental observation that the "plateau" extends to 5K for a wide range of materials and frequencies [30].

It is clear from our results that stress and not hydrogen content is the origin of the anomalously low Q^{-1} that we observe in high stress silicon nitride. Liu and co-authors observed a much lower dissipation in HWCVD a-Si than in e-beam deposited a-Si and Si+ implanted a-Si [5] and attributed this difference to the hydrogen incorporated in the a-Si films by the HWCVD process. This added

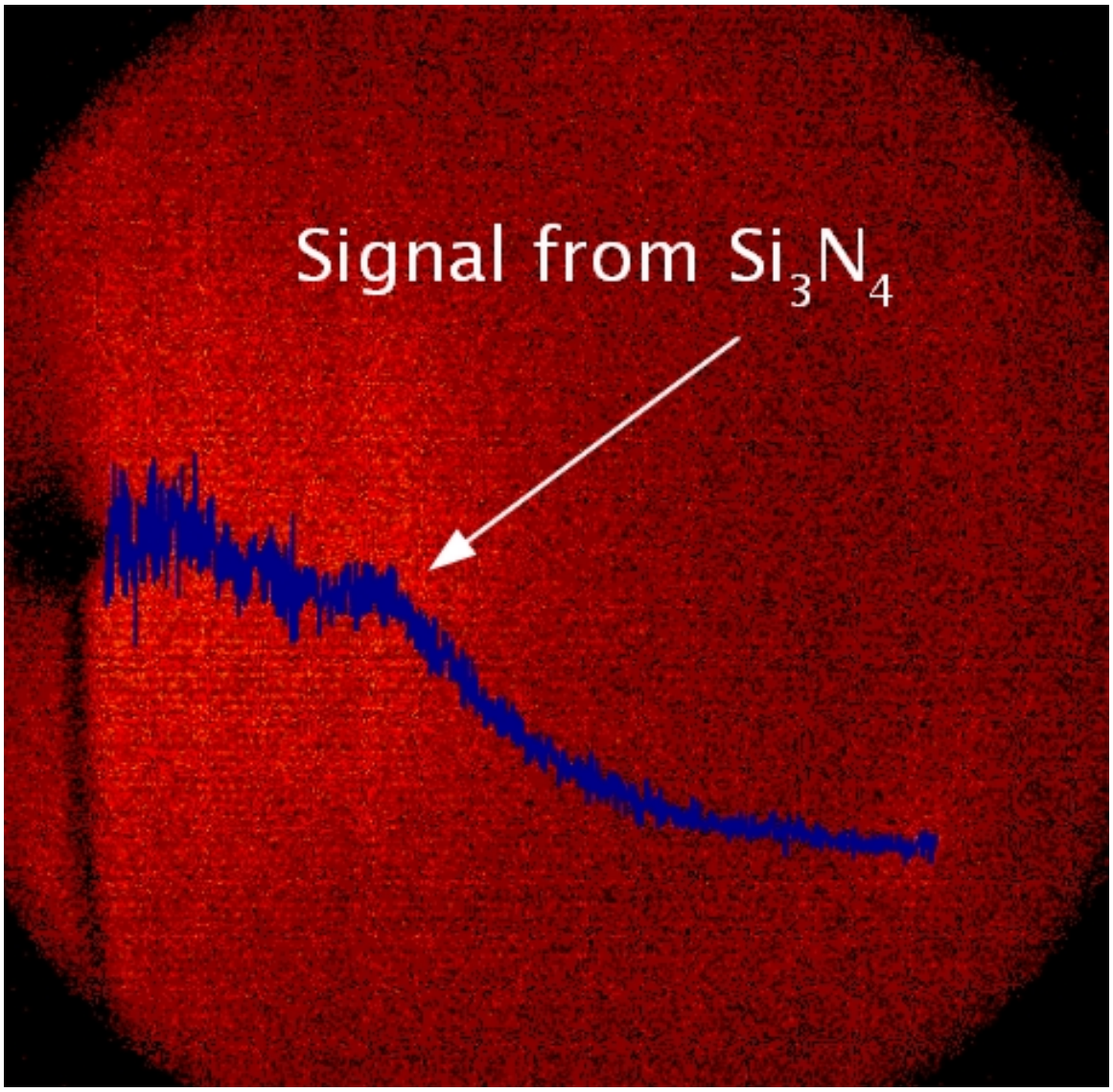

Figure 5.5: General Area Detector Diffraction System (GADDS) image depicts a broad ring at small angles indicative of short range order over size scales up to several nanometers, indicative of glassy character.

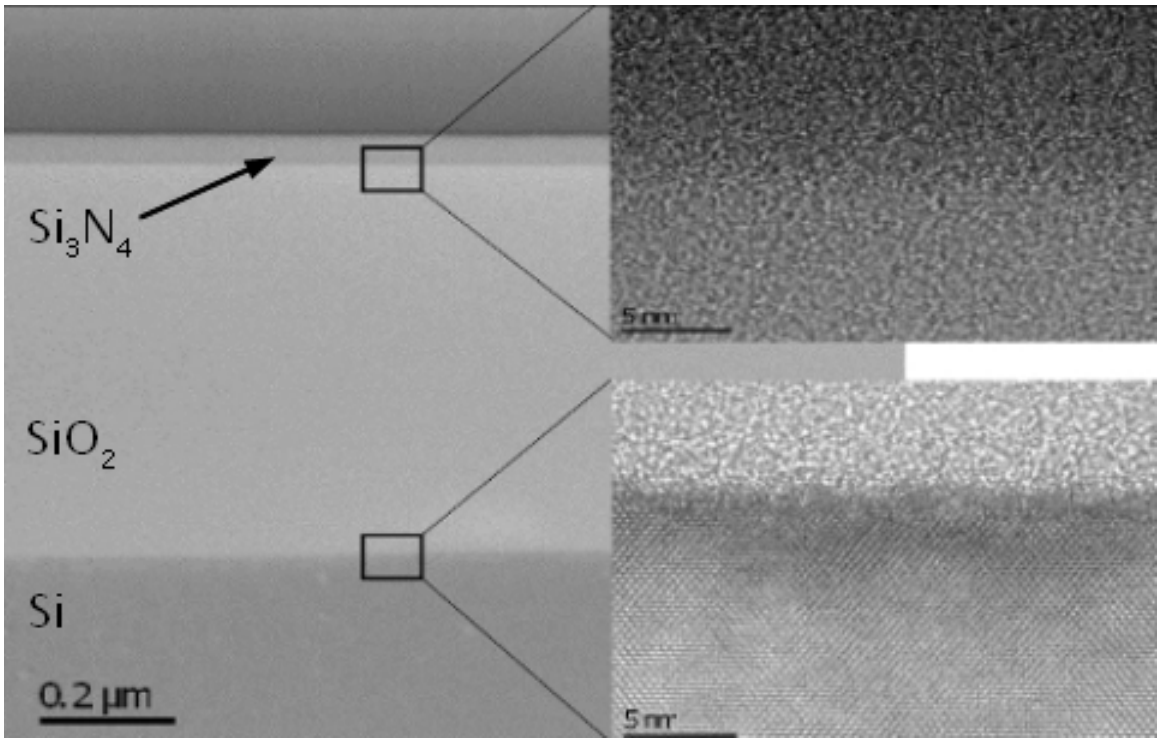

Figure 5.6: High resolution TEM images showing no long range order in the SiO_2 or Si_3N_4 in contrast to the Si lattice.

hydrogen results in a Q^{-1} comparable to those seen in our high-stress silicon nitride resonators. It was conjectured that the hydrogen might lead to the formation of an amorphous network with more perfect fourfold coordination [5]. As noted in one of the original tunneling model papers, the high coordination number that accompanies tetrahedral bonding is expected to inhibit the tunneling process, thus decreasing the density of tunneling states [4]. However, four-fold coordination does not guarantee low Q^{-1} [31]. Silicon nitride also has four-fold coordination and is a candidate for a correspondingly lower dissipation at the plateau. We compare resonators fabricated from identical films, with similar chemical composition [32] and coordination number, with stress being the sole distinguishing factor. Thus hydrogen or coordination number alone cannot be responsible for the anomalously low dissipation observed in the high-stress material. Regardless of the origin, one

comes to the conclusion that either the spectral density $\overline{P}$ or the coupling energy γ must be radically altered by the application of stress.

We offer the following conjectures that would have to be tested. We note that all of the films considered here (in our lab and elsewhere) range from 30 nm to 2 μm thick; thus they have enhanced surface to volume ratios compared to conventional macroscopic resonators. At first sight, the quasi two-dimensional nature of the structures should be important since the availability of nearby sites for tunneling would be different for surface atoms. Yet it was shown in [33] that the Q^{-1} plateau levels in a-SiO_2 films as thin as 0.75 nm are nearly the same as in bulk a-SiO_2 (while Q^{-1} at $T > 10$ K was modified from bulk). So surfaces alone do not alter Q^{-1}. An understanding of the effect of stress could come from two-site models where it is thought that most of the tunneling entities reside on *internal* surfaces (nanovoids) in the glass [34, 35]. Such nanovoids' contours might be more distorted by stress, affecting the tunneling between nearby sites.

The second conjecture relates to the significant departures from the accepted "universal" behavior seen by Liu and coworkers [5, 6] in thin film materials deposited onto a bulk Si substrate. Since the thermal expansion relative to deposition temperature is likely to be different in the film and in the Si/SiO_2 underlayer, the result is either tensile or compressive stress in the film, both of which can lead to higher Q [24, 36]. If this conjecture is correct, then the source of the departure from universal behavior in all of these (few) cases can be traced to the presence of stress. Assuming a flat distribution of $\overline{P}$, $\gamma = 1eV$, a small static strain would not affect Q^{-1} since it would simply perturb the asymmetry of a tunneling state by an amount $\sim$1 eV $\times$ strain. However, in high-stress nitride, the strain (=stress/bulk modulus) $\sim$ 0.007. Thus the strain energy is of order 70 K. The plateau in Q^{-1}, the linear heat capacity, and the quadratic thermal conductivity all set in below

10 K. Thus it is possible that by applying strain a significantly altered region of the distribution is being accessed.

5.5 Conclusion

Regardless of the origin of these effects, whether due to sensitivity of the spectral density or the coupling energy to stress, or because of the effect of stress on tunneling entities confined to surfaces in the form of nanovoids, it is obvious that further work is needed to determine the origin of this non-universal behavior. An important question is whether similar stress-sensitive changes will be seen in conventional glassy materials, especially in the related dielectric properties. Will the hallmarks of universal glassy behavior, the T-linear specific heat and T^2 thermal conductivity [1], be observed in high-stress Si_3N_4 and are these quantities affected by stress? We also hope that this result provokes new experimental and theoretical efforts aimed toward understanding the effect of stress on dissipative processes in glass.[2]

[2]We acknowledge support from: the NSF under DMR-0457533, through the Cornell Materials Science Center under DMR 0520404, and through the IGERT program under DGE-0654193; from Analog Devices and DARPA under HR0011-06-1-0042. Help with various characterization steps is also acknowledged (J. Mundy, M. Thomas, D. Muller: TEM and CBED studies), (M. Weathers, GADDS). We also acknowledge input from J. Saunders, M. Zalalutdinov, R.O. Pohl and R. Kühn.

BIBLIOGRAPHY

[1] R.C. Zeller, and R.O. Pohl, Phys. Rev. B **4**, 2029 (1971).

[2] R.O. Pohl, Xiao Liu, and E. Thompson, Rev. Mod. Phys. **74**, 991 (2002).

[3] P. Anderson, B. Halperin, and C. Varma, Philos. Mag. **25**, 1 (1972).

[4] W.A. Phillips, J. Low Temp. Phys. **7**, 351 (1972).

[5] X. Liu, B.E. White, Jr., R.O. Pohl, E. Iwanizcko, K.M. Jones, A.H. Mahan, B.N. Nelson, R.S. Crandall, and S. Veprek, Phys. Rev. Lett. **78**, 4418 (1997).

[6] X. Liu, T.H. Metcalf, Q. Wang, and D.M. Photiadis, MRS Proc. Amorph. and Polycryst. Thin-Film Silicon Sci. and Techn.-2007 **989**, 511 (2007).

[7] J.D. Thompson, B.M. Zwickl, A.M. Jayich, F. Marquardt, S.M. Girvin and J.G.E. Harris, Nature **452**, 72 (2008), B.M. Zwickl, W.E. Shanks, A.M. Jayich, C. Yang, A.C. Bleszynski Jacyich, J.D. Thompson and J.G.E. Harris, Appl. Phys. Lett., **92**, 103125 (2008).

[8] S.S. Verbridge, H.G. Craighead, and J.M. Parpia, App. Phys. Lett. **92**, 013112 (2008).

[9] K. Schwab, 25th Intl. Conf. on Low Temp. Phys. Amsterdam Aug. 2008.

[10] C.C. Yu and A.J. Leggett, Comments Condens. Matter Phys. **14** 231 (1988).

[11] A.L. Burin and Y. Kagan, Zh. Eksp. Teor. Fiz. **82**, 159 (1996) [Sov. Phys. JETP **82**, 159 (1996)].

[12] R. Kühn, Europhys. Lett. **62**, 313 (2003).

[13] A.D. Fefferman, R.O. Pohl, A.T. Zehnder, and J.M. Parpia, Phys. Rev. Lett. **100**, 195501 (2008).

[14] J. Classen, T. Burkert, C. Enss, and S. Hunklinger, Phys. Rev. Lett. **84**, 2176 (2000).

[15] D.J. Salvino, S. Rogge, B. Tigner, and D.D. Osheroff, Phys. Rev. Lett. **73**, 268 (1994).

[16] S. Rogge, D. Natelson, and D.D. Osheroff, Phys. Rev. Lett. **76**, 3136 (1996).

[17] H.M. Carruzzo, E.R. Grannan and C.C. Yu, Phys. Rev. B **50**, 6685 (1994).

[18] A.L. Burin, J. Low Temp. Phys. **100**, 309 (1995).

[19] D. Natelson, D. Rosenberg, and D.D. Osheroff, Phys. Rev. Lett. **80**, 4689 (1998).

[20] P. Strehlow, C. Enss, and S. Hunklinger, Phys. Rev. Lett. **80**, 5361 (1998).

[21] M. Wohlfahrt, P. Strehlow, C. Enss, and S. Hunklinger, Europhys. Lett. **56**, 690 (2001).

[22] S. Ludwig, C. Enss, P. Strehlow, and S. Hunklinger, Phys. Rev. Lett. **88**, 075501 (2002).

[23] S.S. Verbridge, L.M. Bellan, R.B. Reichenbach, J.M. Parpia, and H.G. Craighead, J. of App. Phys. **99**, 124304 (2006).

[24] S.S. Verbridge, D. Finkelstein-Shapiro, H.G. Craighead, and J.M. Parpia. Nano Lett. **7**, 1728 (2007).

[25] At resonance the maximum motion occurs the center of the membrane or at the cantilever tip. The laser was focussed at or near these points during the measurements.

[26] E.I. Bromley, J.N. Randall, D.C. Flanders and R.W. Mountain, J.Vac. Sci. Technol. B **1**, 1364 (1983).

[27] Y. Miyagawa, T. Murata, Y. Nishida, T. Nakai, A. Uedono, N. Hattori, M. Matsuura, M. Yoneda, Jap. J of Appl. Phys. **46**, 1984 (2007).

[28] M. Zalalutdinov, A. Olkhovets, A. Zehnder, B. Ilic, D. Czaplewski, H. G. Craighead, and J. M. Parpia, Appl. Phys. Lett. **78**, 3142 (2001).

[29] Attocube systems AG, Koniginstrasse 11a RGB, D-80539 Munich, Germany.

[30] K.A. Topp and D.G. Cahill, Z. Phys. B **101**, 235 (1996).

[31] D.A. Czaplewski, J.P. Sullivan, T.A. Friedman, D.W. Carr, B.E.N. Keeler and J.R. Wendt, J. of App. Phys. **97**, 023517 (2005).

[32] Both resonator types had similar exposure to HF that might introduce hydrogen into the film.

[33] B.E. White, Jr. and R.O. Pohl, Phys. Rev. Lett. **75**, 4437 (1995).

[34] J.C. Phillips, Phys. Rev. B. **24**, 1744 (1981).

[35] J.C. Phillips, J. Non-Cryst. Sol. **43**, 37 (1981).

[36] S.S. Verbridge, Ph.D. Thesis, Cornell University (2008).

CHAPTER 6

CONCLUSION AND FUTURE WORK

Development of resonant microtechnology for sensing is still in its infancy, and many challenges remain to be surmounted before large scale deployment can be feasible. This section offers suggestions of next steps in the projects presented in this thesis.

• Elastic squeeze film damping was shown in Chapter 3 to trap a film of gas between the vibrating member and the nearby substrate. It was hypothesized that viscous losses are minimized in such a clamped film because gas within the viscous penetration depth does not undergo viscous flow. Furthermore, it calculated that sound radiation from the top surface would lead to the dissipation observed, suggesting that radiative losses are minimal to the elastic squeeze film.

The implication of these observations, which would have to be tested, is that acoustic radiation from the top surface could likewise be suppressed if another surface were brought within its viscous penetration depth. In that case, the dominant energy loss mechanism could be suppressed, leading to a significant increase in the quality factor.

This could provide an interesting and valuable avenue to ambient operation of resonant MEMS sensors. Clamping the gas film on both surfaces of a drum does not require that the cavity be sealed at the edges. As such, the enhanced-Q resonator would still maintain exposure to ambient gases. Maintaining high quality factor in air could allow some of the great sensitivity of resonant microstructures to be applied outside of laboratory conditions.

Resonant microscale membranes have been shown to act as linear pressure sensors over the range of 10 Torr to above three time atmospheric pressure.

• Stress-based vapor sensing with resonant buckled-beam MEMS exploits the non-linearity of the stress-frequency relationship in these structures. Near the critical buckling load, relatively small changes in stress manifest in significant frequency variation. As such, the sensitivity to changes in the stress of a trace vapor sensitive surface coating was demonstrated in Chapter 4.

A more detailed investigation of the behavior of beams near the critical buckling stress is warranted. Mathematically, the slope of the stress-frequency curve approaches infinite at the critical load, although is known to be smoothed as a result of geometrical imperfections of real devices. However, the limits of sensitivity of this geometry have yet to be explored.

In one possible approach, resonator arrays of varying length could be fabricated in a mildly compressive film. The range of lengths should be chosen so as to assure that buckling occurs at some intermediate length (long beams will buckle under lesser load than otherwise-equivalent shorter beams). A surface coating could then be applied, for example the hygroscopic TBC6A demonstrated in this thesis, and by varying the humidity the buckling behavior of beams of some length should be be observable, and the limits of predictability by the model described in Chapter 4 characterized.

Looking further ahead, once appropriate buckling loads (lengths) for beams were established to match the deposition stresses of a number of sensitive materials, comparative response to analytes could then be made, potentially enabling highly sensitive "fingerprinting" of gas species. Such "electronic" nose technology could be useful in identification of explosive vapors, as well as in identification of various compounds in breath gas for purposes of medical diagnostics.

Resonant microscale buckled bridge structures have been shown here to act as sensitive, non-linear stress sensor and represent a generic platform for trace vapor

sensing.

• The many resonator applications that can make use of high Q (high stress) silicon nitride commend this material to further study in general. The exact roll of stress on dissipation has yet to be determined, as discussed in Chapter 5. Cooling suspended films to temperatures below those of the universal dissipation plateau for glassy materials would reveal whether further departures from the usual behavior of glassy solids, in particular the T-linear specific heat and T^2 thermal conductivity.

In order to cool our silicon nitride resonators below 2 K, the laser heating encountered in Chapter 5 will have to be addressed. New designs for the optical system are currently being explored, but electrical drive and detection could also be considered, as per Chapter 2. This would involve the partial metalization of a silicon nitride membrane.

Another important investigation will be whether other glassy materials under high tensile stress exhibit the same high-Q behavior. Silicon nitride is not unique in its ability to withstand tremendous tension. As discussed in Chapter 1, high quality ceramic films withstand tensile loads many fold in excess of the fracture strength of the bulk material. For example, the thermal oxide used in these experiments could be patterned and released in potassium hydroxide and mechanically tensioned by wafer bending. Were the same effect observed, then a model based on stored energy and the stress-dependence of the per-cycle loss could be pursued. If the per-cycle dissipation were not to scale with stress to an identical degree as the energy stored in tension, then the microscopic losses involved in bending or elongation of the structure would direct further investigated.

Here we show that resonators made from glassy high-stress silicon nitride exhibit dissipation far lower than the current understanding of amorphous materials allows. This finding represents an opportunity to study dissipation and its rela-

tionship to stress in materials.

• Parametric amplification has been shown to narrow the resonance width of micromechanics, but is believed not to improve the overall sensitivity of resonators since the peak instability offsets improvements in the Q. This, however, should be experimentally verified for the electrical drive and detection scheme described in Chapter 2. Parametric signal amplification with the appropriate phase dependencies was confirmed by experiment, however no qualitative narrowing of the resonance was observed.

However, in the experience of the author, parametrically driven resonators produced clearer signals at higher pressures than resonators capacitively driven at their resonance frequency. Given the great experimental and practical value of resonant MEMS operating in ambient conditions, this effect should be investigated further.

A final, potentially valuable effect observed in MEMS resonators operated by the electrical means of Chapter 2 is self-oscillation. Though the time frame of these studies did not permit a detailed investigation, the author has on numerous occasions observed large resonance with large signal strength resulting from only noise and DC drive. The effect could be observed without AC drive in a several volt bound range of DC tensions (e.g. $21 < V_{DC} < 23$). The feedback mechanism necessary for maintenance of self-oscillation has yet to be determined, but given the large signal and obvious value of DC-only actuation, the effect could be extremely valuable and further study is warranted.

We demonstrate a compact and fully electrical method of resonator readout in several sensing contexts. This method represents a robust and efficient detection scheme for applied resonant sensor technology.

Miniaturization mechanical resonators may not necessarily be the best or only way to meet the need for advanced sensor technology. The advantages, calculated and demonstrated, face yet-unresolved challenges in application outside of the laboratory. Maintenance of high quality resonance in fluid and understanding the effects of environmental variable will require continued investigation, innovation, and effort. It is hoped, however, that the great potential and sensitivity of microscale resonant sensor technology stimulate solutions to the current challenges, assisted in some small part by the work presented in this thesis. As these challenges are overcome, new insights, applications, and innovation may emerge from this fascinating field of applied science.

APPENDIX A

FILM PREPARATION

This section contains details of device fabrication focusing on film recipes and processing details germane for those wishing to recreate the devices described in this thesis. All films are grown at the Cornell Nanofabrication Facility.

All resonant devices described in this thesis were released by means of removing the SiO_2 film underlying the device layer, usually by a wet release in hydrofluoric acid, HF. The oxide films are grown as follows.

A.1 Thermal Oxide

Bare, conductive silicon handle wafers—usually N^+-doped—are rigorously cleaned (MOS-standard cleaning). This hot-base-hot-acid cleaning is followed by a brief (20 second) dip into dilute (20:1) HF to remove the native oxide before the wafers are transferred to the oxide furnace. Oxide is grown at 1000 °C in the wet HCl process.

During oxide growth, silicon is transformed due to diffusion of oxygen into the silicon crystal lattice. As such, the rate of oxide growth is highly thickness dependent. This is illustrated by the time required to grow the three thicknesses of oxide described in Chapter 3, where the 95, 223, and 665 nm films required respectively 10, 30, and 150 minutes of growth.

A.2 Tensile Polycrystalline Silicon

The typical recipe is for N^+-doped films (phosphorous doping, introducing additional electrons to the lattice). Doped films were chosen for device layer conductivity. Films were grown at a temperature of 590° at 250 mTorr, which deposits

at nominally 3.5–4.0 $^{nm}/_{min}$.

A.3 Compressive Polycrystalline Silicon

Compressively-stressed polycrystalline silicon films were used in the fabrication of the buckled beam resonators described in Chapter 4. The recipe for films is identical to that of the tensile films described in Section A.2. The salient difference is merely the layer thickness: The compressive films in Chapter 4 are 130 nm in thickness, as measured by a FilmMetric thickness measurement system and verified by profilometry (P-10 Profilometer).

Due to the details of Volmer-Weber island growth processes the inherent stress tends to greater included tensile stress with increasing film thickness. Briefly, the greater surface energy doe to the high radius of curvature of small islands repels neighboring islands. As films increase in thickness, bulk properties overwhelm this effect. For this recipe on standard silicon wafers the compressive-tensile transition occurs between 130 nm and 400 nm.

APPENDIX B

FULL LIST OF FILM RECIPES

All of the polysilicon films in this thesis are created from phosphorous-doped (N^+) polysilicon. A full list of film recipes is included below.

Table B.1: Film recipes

Process	**Temperature**	**Time and Thickness**	**Result**
150 mTorr N^+ Poly	600°	110 nm	compressive
150 mTorr N^+ Poly	590°	220 nm	compressive
250 mTorr N^+ Poly	610°	90 min, 85 nm	compressive
250 mTorr N^+ Poly	590°	100 min, 328 nm	tensile
250 mTorr N^+ Poly	590°	32 min, 116-130 nm	compressive
250 mTorr N^+ Poly	570°	86 nm	very compressive
Undoped Poly	580°	70 min, nm	compressive

APPENDIX C

SPICE MODEL OF AN INDUCTOR

The non-idealities in the behavior of real inductors are is relevant to impedance matching. A more realistic model is given in Figure C.

The value of the equivalent complex impedance is

$$Z_{equiv} = R2 + [\frac{1}{R_1 - \frac{i}{\omega C}} = \frac{1}{R_{var} + j\omega L}]^{-1} \tag{C.1}$$

where $R_{var} = k\sqrt{f}$, and k is a measured value in the inductor specifications.

For example, the inductor in Example #2, Section 2.3.3, is a Coilcraft 1812LS-473 chip inductor whose specifications are given in Table C.1.

Plugging these values into Equation C.1 (assuming $F_0 = 8.45$ MHz) yields $Z_{equiv} = 40 + i2513\ \Omega$, which can be thought of as a series real resistor and ideal inductor. The real impedance, the 40 Ω represents a significant portion of the total system impedance, $Z(\omega)$.

Note also that the quality factor (frequency width) of the tank resonance is given by $Q_{tank} = \frac{\mathbb{I}(Z_L)}{\mathbb{R}(Z_L)} = \frac{2513}{40} = 63$.

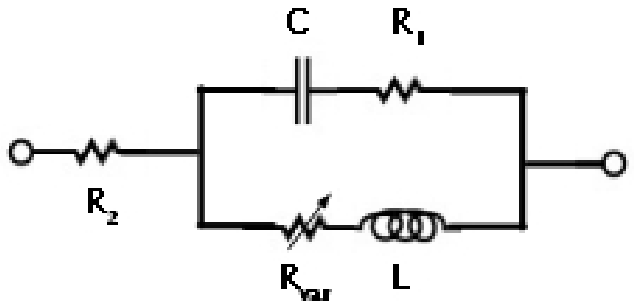

Figure C.1: Lumped element model of a real inductor

Table C.1: Exemplary Inductor Parameters

R_1	408 Ω
R_2	5.0 Ω
C	0.92 pF
L	47 μH
k	9.93×10^{-3}